



# A lattice Boltzmann model for multiphase flows with moving contact line and variable density

Jizu Huang<sup>a,b</sup>, Xiao-Ping Wang<sup>c,\*</sup>

<sup>a</sup> LSEC, Institute of Computational Mathematics and Scientific/Engineering Computing, Academy of Mathematics and Systems Science, Chinese Academy of Sciences, Beijing 100190, China

<sup>b</sup> School of Mathematical Sciences, University of Chinese Academy of Sciences, Beijing 100049, China

<sup>c</sup> Department of Mathematics, The Hong Kong University of Science and Technology, Clear Water Bay, Kowloon, Hong Kong, China

## ARTICLE INFO

### Article history:

Received 15 February 2016

Received in revised form 31 August 2017

Accepted 2 October 2017

Available online 12 October 2017

### Keywords:

Lattice Boltzmann model

Variable density

Moving contact line

Slip boundary condition

## ABSTRACT

In this paper, we develop an efficient lattice Boltzmann model for the two-phase moving contact line problem with variable density. The Navier–Stokes and Cahn–Hilliard equations are recovered from the lattice Boltzmann model proposed by Fakhari and Rahimian [5]. To improve numerical stability, we present a semi-implicit lattice Boltzmann method together with a mixed finite difference scheme. In order to describe the behavior of the contact line motion on the boundary, we incorporate the generalized Navier boundary condition [25] by the nonequilibrium extrapolation method [8]. The proposed method is easy to implement and retains the advantage of the standard lattice Boltzmann method. Numerical tests are carried out to verify the proposed method. Our numerical results show that the present approach is able to model two-phase flows with variable density and moving contact line.

© 2017 Elsevier Inc. All rights reserved.

## 1. Introduction

Modelling and simulation of multiphase and multi-component flows have attracted a lot of attentions in recent years. The moving contact line problem, where the fluid–fluid interface intersects the solid wall, is one of the most difficult and important problems that still under intensive investigations. It is well known that the Navier–Stokes equation coupled with no-slip boundary condition will lead to a non-physical singularity near the moving contact line [4]. A phase field model with the generalized Navier boundary condition (GNBC) is proposed in [25] for the moving contact line problem. It is shown that the numerical results based on the GNBC can reproduce quantitatively the results from the MD simulation. The GNBC is also used in different moving contact line problems successfully [21,33]. Several efficient numerical methods are also developed in recent years for the coupled Navier–Stokes equations and Cahn–Hilliard equation with the GNBC [2,6,7,9].

Recently, the lattice Boltzmann method (LBM) has been developed as an alternative and promising numerical scheme for simulating multiphase and multi-component flows. By taking the interface as a transition layer (diffuse interface), several models in lattice Boltzmann context [10,27,28,31] are developed for multiphase and multi-component flows. In those methods, the density ratio usually cannot be very large due to numerical instability. To overcome this difficulty, several new methods are proposed for multiphase and multi-component flows with large density ratio. In [11], Inamuro et al. introduce a model based on the free energy method for multiphase and multi-component flows with large density ratio. Lee and Lin [17] develop a stabilized scheme of discrete Boltzmann equations for multiphase flows with large density ratio. However, in

\* Corresponding author.

E-mail address: mawang@ust.hk (X.-P. Wang).

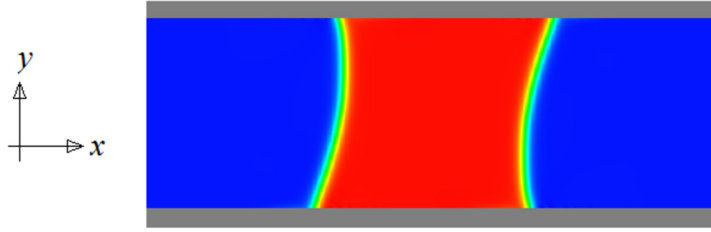


Fig. 1. Two phase channel flow.

the above two methods, the Cahn–Hilliard equation cannot be completely recovered from the lattice Boltzmann equations. A different approach is proposed in [37] to recover the Cahn–Hilliard equation without any additional terms. Because the effect of local density variation is not considered in the continuity and momentum equations, the model proposed in [37] is unable to consider the effect of density contrast as pointed out by Fakhari and Rahimian [5]. To simulate multiphase flows with the effect of the local density in the continuity and momentum equations, several models are presented in [5,29,30,34,35]. In [19,20], Li et al. propose a lattice Boltzmann model with an improved pseudopotential model for multiphase flows at large density ratio. Based on it, an improved forcing scheme is presented to simulate multiphase flows at arbitrarily high density ratios in [22] and a cascaded lattice Boltzmann method with the improved forcing scheme is introduced to simulate large-density-ratio multiphase flows at high Reynolds numbers and Weber numbers [18,23].

So far, only few phase field model based on LBM can treat the moving contact line problem. In this paper, we aim to simulate the moving contact line problem using the lattice Boltzmann model. On the solid wall, the macroscopic variables are set to satisfy the GNBC and a relaxation boundary condition. The density distribution functions are then obtained by the nonequilibrium extrapolation method (NEM) [8] from the macroscopic variables. The remainder of the paper is organized as follows. In section 2, a phase field model with the GNBC is considered for moving contact line problem. In section 3, we introduce a lattice Boltzmann model for multiphase flows with moving contact line and variable density. The implement of the GNBC and the relaxation boundary condition is also discussed in the same section. Several numerical results are reported in section 4 and concluding remarks are given in section 5.

## 2. Phase field model with moving contact line and variable density

In this section, we introduce a phase field model for moving contact line problem with the GNBC [25,26]. In the model, the multiphase flows are set to satisfy the following Cahn–Hilliard and Navier–Stokes equations

$$\begin{cases} \nabla \cdot \mathbf{u} = 0, \\ n \left[ \frac{\partial \mathbf{u}}{\partial t} + (\mathbf{u} \cdot \nabla) \mathbf{u} \right] = -\nabla p + \nabla [\eta (\nabla \mathbf{u} + (\nabla \mathbf{u})^T)] + \mathbf{G}_{\text{ext}} + \mu \nabla \phi, \\ \frac{\partial \phi}{\partial t} + \nabla \cdot (\phi \mathbf{u}) = \theta_M \nabla^2 \mu, \end{cases} \quad (1)$$

where  $p$  is the pressure,  $n$ ,  $\eta$  are the fluid mass density and dynamic viscosity,  $\mathbf{u} = (u_x, u_y)^T$  and  $\phi$  are the fluid velocity and order parameter;  $\mathbf{G}_{\text{ext}}$  is the external body force, and  $\theta_M$  is the phenomenological mobility coefficient. Here  $\mu$  is the chemical potential, and  $\mu \nabla \phi$  is the capillary force. For a channel flow (as shown in Fig. 1), the GNBC on the top and bottom walls is defined as

$$\hat{\beta} u_x^{\text{slip}} = -\eta \partial_{\mathbf{n}} u_x + \hat{L}(\phi) \partial_x \phi, \quad (2)$$

where  $\hat{L}(\phi) = \kappa \partial_{\mathbf{n}} \phi + \partial \gamma_{wf}(\phi) / \partial \phi$ , and  $\gamma_{wf}(\phi) = -\frac{1}{2} \gamma \cos(\theta^{\text{surf}}) \sin(\frac{\pi}{2} \phi)$ . Here  $\theta^{\text{surf}}$  is the static contact angle,  $\hat{\beta}$  is the slip coefficient,  $u_x^{\text{slip}} = u_x - u_w$  is the slip velocity,  $u_w$  is the wall speed, and  $\mathbf{n}$  is the unit vector orthogonal to the boundaries.  $\kappa$  is a parameter related to the interface profile thickness  $\xi$  and the interfacial tension  $\gamma$ . A relaxation boundary condition is imposed on the order parameter  $\phi$  at the top and bottom boundaries

$$\frac{\partial \phi}{\partial t} + u_x \partial_x \phi = -\hat{\Lambda} [\hat{L}(\phi)], \quad (3)$$

where  $\hat{\Lambda}$  is a (positive) phenomenological parameter, together with the following impermeability conditions

$$u_y = 0, \quad \partial_{\mathbf{n}} \mu = 0. \quad (4)$$

Here the variable density and viscosity are taken to be the volume average of those for the two flows, i.e.,

$$n = n_L \left( \frac{1 + \phi}{2} \right) + n_G \left( \frac{1 - \phi}{2} \right), \quad \eta = \eta_L \left( \frac{1 + \phi}{2} \right) + \eta_G \left( \frac{1 - \phi}{2} \right).$$

Here  $n_L$  and  $n_G$  denote the liquid density and gas density,  $\eta_L$  and  $\eta_G$  denote the liquid dynamic viscosity and gas dynamic viscosity, respectively.

### 3. The lattice Boltzmann model for moving contact line problem

#### 3.1. The interface capture equation

In order to recover Cahn–Hilliard equation, we introduce a lattice Boltzmann equations in the D2Q9 model [5]

$$\frac{\partial g_\alpha(\mathbf{x}, t)}{\partial t} + \mathbf{e}_\alpha \cdot \nabla g_\alpha(\mathbf{x}, t) = \Omega_\alpha^g(\mathbf{x}, t), \quad \alpha = 0, 1, \dots, 8, \quad (5)$$

with BGK approximation of the collision term [3]

$$\Omega_\alpha^g(\mathbf{x}, t) = \frac{g_\alpha^{(eq)}(\mathbf{x}, t) - g_\alpha(\mathbf{x}, t)}{\tau_\phi}, \quad (6)$$

where  $g_\alpha$  is the order parameter distribution function,  $\mathbf{e}_\alpha = (e_{\alpha 1}, e_{\alpha 2})^T$  is the lattice velocity, and  $\tau_\phi$  is the single relaxation parameter. The discrete velocities are defined by  $\mathbf{e}_0 = (0, 0)$ , and  $\mathbf{e}_\alpha = \lambda_\alpha (\cos \theta_\alpha, \sin \theta_\alpha)$ , with  $\lambda_\alpha = 1$ ,  $\theta_\alpha = (\alpha - 1)\pi/2$  for  $\alpha = 1, 2, 3, 4$ , and  $\lambda_\alpha = \sqrt{2}$ ,  $\theta_\alpha = (\alpha - 5)\pi/2 + \pi/4$  for  $\alpha = 5, 6, 7, 8$ . The order parameter  $\phi$  is calculated by

$$\phi = \sum_\alpha g_\alpha. \quad (7)$$

The equilibrium distribution functions in (6) can be expressed as follows

$$g_\alpha^{(eq)} = \begin{cases} \phi - 3\mu\Gamma(1 - w_0), & \alpha = 0, \\ 3w_\alpha[\mu\Gamma + \phi(\mathbf{e}_\alpha \cdot \mathbf{u})], & \alpha = 1, 2, \dots, 8, \end{cases} \quad (8)$$

where  $\Gamma$  is a parameter to control the mobility. The weight coefficients  $w_\alpha$  are given by

$$w_0 = 4/9, \quad w_\alpha|_{\alpha=1,2,3,4} = 1/9, \quad w_\alpha|_{\alpha=5,6,7,8} = 1/36. \quad (9)$$

To improve numerical stability, we introduce a semi-implicit lattice Boltzmann method to discretize equation (5) along characteristics over time step  $\Delta t$ . The discretized system for the interface capture equation is

$$g_\alpha(\mathbf{x} + \Delta t \mathbf{e}_\alpha, t + \Delta t) - g_\alpha(\mathbf{x}, t) = \frac{\Delta t}{2} (\Omega_\alpha^g(\mathbf{x}, t) + \Omega_\alpha^g(\mathbf{x} + \Delta t \mathbf{e}_\alpha, t + \Delta t)), \quad \alpha = 0, 1, \dots, 8. \quad (10)$$

More details about numerical implementation of the discretized system are given in Section 3.3.

#### 3.2. The continuity and momentum equations

To simulate multiphase flows with variable density contrast, we use the multiple-relaxation-time (MRT) lattice Boltzmann model of Fakhari and Rahimian [5], which is developed to correct the model of Zheng et al. [37]. In the lattice Boltzmann model of Zheng et al. [37], the particle distribution function is used to calculate the mean density and velocity with high efficiency and stability. However, it cannot properly consider the effect of the local density in the continuity and momentum equations. To correctly consider the effect of the local density in the momentum equations, several models are presented in [5,29,30]. In this paper, we use the model proposed by Fakhari and Rahimian [5] to implement the continuity and momentum equations, in which the local density is considered by using a pressure evolution based on the MRT lattice Boltzmann model. The lattice Boltzmann implementation of Navier–Stokes equations [5] can be written as follows

$$f_\alpha(\mathbf{x} + \Delta t \mathbf{e}_\alpha, t + \Delta t) - f_\alpha(\mathbf{x}, t) = \Omega_\alpha^f, \quad \alpha = 0, 1, \dots, 8, \quad (11)$$

with the BGK approximation of the collision term

$$\Omega_\alpha^f(\mathbf{x}, t) = \left\{ \frac{f_\alpha^{(eq)}(\mathbf{x}, t) - f_\alpha(\mathbf{x}, t)}{\tau_n} + \left(1 - \frac{1}{2\tau_n}\right) \mathcal{F}_\alpha(\mathbf{x}, t) \right\}, \quad (12)$$

where  $\tau_n$  is the single relaxation time and

$$\mathcal{F}_\alpha(\mathbf{x}, t) = \Delta t \frac{(\mathbf{e}_\alpha - \mathbf{u})}{c_s^2} \left[ c_s^2 (\zeta_\alpha - w_\alpha) \nabla n + \zeta_\alpha (\mu \nabla \phi + \mathbf{G}_{\text{ext}}) \right]. \quad (13)$$

Here  $c_s = 1/\sqrt{3}$  is the speed of sound,  $\zeta_\alpha$  is set as  $w_\alpha \left[ 1 + \frac{\mathbf{e}_\alpha \cdot \mathbf{u}}{c_s^2} + \frac{(\mathbf{e}_\alpha \cdot \mathbf{u})^2}{2c_s^4} - \frac{|\mathbf{u}|^2}{2c_s^2} \right]$ , and  $n$  is the local density. Moreover,  $f_\alpha(\mathbf{x}, t)$  and  $f_\alpha^{(eq)}(\mathbf{x}, t)$  are the particle distribution functions and equilibrium particle distribution functions, respectively. The equilibrium distribution functions are given as follows [5]

$$f_\alpha^{(eq)}(\mathbf{x}, t) = w_\alpha n_0 + w_\alpha n \left( \frac{\mathbf{e}_\alpha \cdot \mathbf{u}}{c_s^2} - \frac{|\mathbf{u}|^2}{2c_s^2} + \frac{(\mathbf{e}_\alpha \cdot \mathbf{u})^2}{2c_s^4} \right), \quad (14)$$

where  $n_0$  denotes the mean density and the pressure  $p = c_s^2 n_0$ . For the D2Q9 discrete lattice model, the coefficients are taken as  $w_0 = 4/9$ ,  $w_\alpha|_{\alpha=1,2,3,4} = 1/9$ ,  $w_\alpha|_{\alpha=5,6,7,8} = 1/36$ . The discrete velocities are defined by  $\mathbf{e}_0 = (0, 0)$ , and  $\mathbf{e}_\alpha = \lambda_\alpha (\cos \theta_\alpha, \sin \theta_\alpha)$ , with  $\lambda_\alpha = 1$ ,  $\theta_\alpha = (\alpha - 1)\pi/2$  for  $\alpha = 1, 2, 3, 4$ , and  $\lambda_\alpha = \sqrt{2}$ ,  $\theta_\alpha = (\alpha - 5)\pi/2 + \pi/4$  for  $\alpha = 5, 6, 7, 8$ .

In the lattice Boltzmann model, the local density  $n$ , velocity  $\mathbf{u}$ , and pressure  $p$  are defined in terms of the distribution functions  $f_\alpha$  [5]

$$\begin{aligned} n &= n_L \left( \frac{\phi + \phi^*}{2\phi^*} \right) + n_G \left( \frac{\phi^* - \phi}{2\phi^*} \right), \\ \mathbf{u} &= \frac{1}{n} \left[ \sum_\alpha f_\alpha \mathbf{e}_\alpha + \frac{\Delta t}{2} (\mu \nabla \phi + \mathbf{G}_{\text{ext}}) \right], \\ p &= c_s^2 n_0 = \sum_\alpha c_s^2 f_\alpha + c_s^2 \frac{\Delta t}{2} \mathbf{u} \cdot \nabla n. \end{aligned} \quad (15)$$

In this model, the mean density  $n_0$  can be initialized by  $(n_L + n_G)/2$ . The local single relaxation parameter  $\tau_n$  is calculated by the local kinematic viscosity  $\nu$  through  $\tau_n = \Delta t \nu / c_s^2 + 0.5$ , where  $\nu$  is determined by the local dynamic viscosity  $\eta$  and the local density  $n$  through  $\nu = \eta / n$ . With the Chapman–Enskog expansion, we derive the Navier–Stokes equations (1) with second-order of accuracy [5].

To simulate the multiphase flows with variable density ratio, a transformation to change the particle distribution  $f_\alpha$  in the velocity space into their counterparts in moment space is defined as

$$\hat{f}_\alpha = \sum_i M_{\alpha i} f_i, \quad \hat{f}_\alpha^{(eq)} = \sum_i M_{\alpha i} f_i^{(eq)}, \quad \hat{\mathcal{F}}_\alpha = \sum_i M_{\alpha i} \mathcal{F}_i, \quad (16)$$

where the transformation matrix  $\mathbf{M}$  is given by [16]

$$M = \begin{bmatrix} 1 & 1 & 1 & 1 & 1 & 1 & 1 & 1 & 1 \\ -4 & -1 & -1 & -1 & -1 & 2 & 2 & 2 & 2 \\ 4 & -2 & -2 & -2 & -2 & 1 & 1 & 1 & 1 \\ 0 & 1 & 0 & -1 & 0 & 1 & -1 & -1 & 1 \\ 0 & -2 & 0 & 2 & 0 & 1 & -1 & -1 & 1 \\ 0 & 0 & 1 & 0 & -1 & 1 & 1 & -1 & -1 \\ 0 & 0 & -2 & 0 & 2 & 1 & 1 & -1 & -1 \\ 0 & 1 & -1 & 1 & -1 & 0 & 0 & 0 & 0 \\ 0 & 0 & 0 & 0 & 0 & 1 & -1 & 1 & -1 \end{bmatrix}. \quad (17)$$

The corresponding MRT lattice Boltzmann equations in the momentum space is

$$\hat{f}_\alpha(\mathbf{x} + \Delta t \mathbf{e}_\alpha, t + \Delta t) - \hat{f}_\alpha(\mathbf{x}, t) = \sum_{i=0}^8 \hat{S}_{\alpha i}^n [\hat{f}_\alpha^{(eq)}(\mathbf{x}, t) - \hat{f}_\alpha(\mathbf{x}, t)] + \hat{\mathcal{F}}_\alpha(\mathbf{x}, t) - \frac{1}{2} \sum_{i=0}^8 \hat{S}_{\alpha i}^n \hat{\mathcal{F}}_i(\mathbf{x}, t). \quad (18)$$

The relaxation matrix  $\hat{\mathbf{S}}^n$  is a diagonal matrix given by  $\hat{\mathbf{S}}^n = \text{diag}(s_0^n, s_1^n, \dots, s_8^n)$ . The parameters are set as  $s_{0,3,5}^n = 1$ ,  $s_1^n = 1.2$ ,  $s_2^n = 1.1$ ,  $s_{7,8}^n = 1/\tau_n$ , and  $s_6^n = s_4^n = 3(2 - s_8^n)/(3 - s_8^n)$ .

The chemical potential  $\mu$  in (8) is derived from the free energy density functional. According to [13,14], the free energy density functional in a closed volume with a mixture of two fluids is defined as

$$F(\phi) = \int \mathcal{F} d\mathbf{x} = \int \left[ \Psi(\phi) + \frac{\kappa}{2} (\nabla \phi)^2 + \frac{n \ln n}{3} \right] d\mathbf{x}, \quad (19)$$

where  $\kappa$  is a coefficient related to the surfacial tension and the interface profile thickness. In the paper, the bulk free energy density per unit mass for the homogeneous system is chosen as a double-well form

$$\Psi(\phi) = A [\phi^2 - (\phi^*)^2]^2,$$

where  $A$  is an amplitude parameter to control the interaction energy between the two phases. The chemical potential is then derived as  $\mu = \frac{\partial \mathcal{F}}{\partial \phi} - \nabla \cdot \frac{\partial \mathcal{F}}{\partial \nabla \phi} = -\kappa \nabla^2 \phi + 4A[\phi^3 - (\phi^*)^2 \phi]$ , where  $\kappa = \frac{3\gamma\xi}{8(\phi^*)^2}$ ,  $A = \frac{3\gamma}{4\xi(\phi^*)^4}$  are the parameters related to the interface profile thickness  $\xi$ , the interfacial tension  $\gamma$ , and the constant  $\phi^* = \frac{n_L - n_G}{2}$ .

The GNBC in the lattice units is described as

$$\beta u_x^{\text{slip}} = -\eta \partial_{\mathbf{n}} u_x + L(\phi) \partial_x \phi / \phi^*, \quad (20)$$

where  $L(\phi) = \kappa \phi^* \partial_{\mathbf{n}} \phi - \frac{\pi\gamma}{4} \cos(\theta^{\text{surf}}) \cos(\frac{\pi\phi}{2\phi^*})$  and  $\beta$  is a parameter related to the slip coefficient. The relaxation boundary condition in the lattice units is

$$\frac{\partial \phi}{\partial t} + u_x \partial_x \phi = -\Lambda L(\phi), \quad (21)$$

where  $\Lambda$  is the phenomenological parameter in the lattice units.

### 3.3. Numerical implementation

The discretized interface capture equation given in the above section can be solved in following three steps.

#### 1. Pre-streaming collision step.

$$\bar{g}_\alpha(\mathbf{x}, t) = g_\alpha(\mathbf{x}, t) + \frac{\Delta t}{2} \Omega_\alpha^g(\mathbf{x}, t), \quad \alpha = 0, 1, \dots, 8. \quad (22)$$

#### 2. Streaming step.

$$\bar{g}_\alpha(\mathbf{x} + \Delta t \mathbf{e}_\alpha, t + \Delta t) = \bar{g}_\alpha(\mathbf{x}, t), \quad \alpha = 0, 1, \dots, 8. \quad (23)$$

#### 3. Post-streaming collision step.

$$g_\alpha(\mathbf{x} + \Delta t \mathbf{e}_\alpha, t + \Delta t) = \bar{g}_\alpha(\mathbf{x} + \Delta t \mathbf{e}_\alpha, t + \Delta t) + \frac{\Delta t}{2} \bar{\Omega}_\alpha^g(\mathbf{x} + \Delta t \mathbf{e}_\alpha, t + \Delta t), \quad \alpha = 0, 1, \dots, 8. \quad (24)$$

In the post-streaming collision step, the collision operator is calculated by the distribution functions  $\bar{g}_\alpha(\mathbf{x} + \Delta t \mathbf{e}_\alpha, t + \Delta t)$ .

Let  $g_\alpha^m(i, j) \approx g_\alpha(\mathbf{x}_{ij}, m)$  and  $f_\alpha^m(i, j) \approx f_\alpha(\mathbf{x}_{ij}, m)$  denote the approximate solutions at the  $m$ th time step. Here  $\mathbf{x}_{ij} = (x_1^i, x_2^j) = (i, j)^T$ ,  $(i, j = 0, 1, \dots, N-1)$ , denote all mesh points in the computational domain.

In the pre-streaming collision step, the collision operator is a function of velocity  $\mathbf{u}$ , which includes the gradient of  $\phi$ . For the purpose of stability, we apply a mixed scheme to discrete the gradient of  $\phi$ . The mixed scheme is combined with a second order central scheme and a second order upwind scheme, which is defined as

$$\frac{\partial \phi}{\partial x_k^i} \Big|_m = \epsilon \frac{\partial \phi}{\partial x_k^i} \Big|_u + (1 - \epsilon) \frac{\partial \phi}{\partial x_k^i} \Big|_c, \quad k = 1, 2, i = 1, 2, \dots, N-2, \quad (25)$$

where  $\frac{\partial \phi}{\partial x_k^i} \Big|_u$  is an upwind scheme,  $\frac{\partial \phi}{\partial x_k^i} \Big|_c$  is a second-order central scheme, and  $\epsilon = 0.5$  is a control parameter to adjust the weights of the two components. Here  $\frac{\partial \phi}{\partial x_k^i} \Big|_u$  and  $\frac{\partial \phi}{\partial x_k^i} \Big|_c$  are respectively defined by

$$\frac{\partial \phi}{\partial x_k^i} \Big|_u = \begin{cases} \frac{1}{2} [3\phi(x_k^i, \cdot) - 4\phi(x_k^{i-1}, \cdot) + \phi(x_k^{i-2}, \cdot)] & \text{if } \mu \phi e_{\alpha k} \leq 0, \\ -\frac{1}{2} [3\phi(x_k^i, \cdot) - 4\phi(x_k^{i+1}, \cdot) + \phi(x_k^{i+2}, \cdot)] & \text{if } \mu \phi e_{\alpha k} > 0, \end{cases}$$

and

$$\frac{\partial \phi}{\partial x_k^i} \Big|_c = \frac{1}{2} [\phi(x_k^{i+1}, \cdot) - \phi(x_k^{i-1}, \cdot)].$$

At the  $m$ th time step, the scheme includes the following three steps:

Step I (Inner points updating): Update the distribution function  $g_\alpha^m(i, j)$  and  $f_\alpha^m(i, j)$ ,  $j = 1, 2, \dots, N-2$ , through the semi-implicit scheme and the MRT lattice Boltzmann method, respectively..

Step II (The boundary macroscopic variables updating): Calculate the order parameter  $\phi^m$  and velocity  $\mathbf{u}^m$  on the boundary from the relaxation boundary condition and the GNBC. The chemical potential  $\mu^m$  and the number density  $n^m$  on the boundary are also updated at this step.

Step III (The boundary points updating): Compute the distribution function  $g_\alpha^m(i, j)$  and  $f_\alpha^m(i, j)$ ,  $j = 0$  or  $N - 1$ , by the NEM [8].

In Step I, we need a numerical approximations of  $\nabla\phi$  and  $\nabla^2\phi$  at each time step. In this paper, a second-order central finite difference scheme and a five points second-order accurate finite difference scheme are used to discrete  $\nabla\phi$  and  $\nabla^2\phi$ , respectively. In Step II, the macroscopic variables on the boundary are updated by the corresponding boundary conditions. For a mesh point  $(i, 0)$  on the bottom wall, the scheme for the order parameter  $\phi^m(i, 0)$  is

$$\phi^m(i, 0) = \phi^{m-1}(i, 0) - u_x^{m-1}(i, 0) \frac{\phi^{m-1}(i+1, 0) - \phi^{m-1}(i-1, 0)}{2} - \Lambda L(\phi^{m-1}(i, 0)). \quad (26)$$

The velocity  $\mathbf{u}^m$  is updated by

$$\begin{aligned} u_x^m(i, 0) &= u_w + \frac{1}{\beta} \left[ -\eta^{m-1}(i, 0) \frac{3u_x^{m-1}(i, 0) - 4u_x^{m-1}(i, 1) + u_x^{m-1}(i, 2)}{2} \right. \\ &\quad \left. + L(\phi^{m-1}(i, 0)) \frac{\phi^{m-1}(i+1, 0) - \phi^{m-1}(i-1, 0)}{2\phi^*} \right], \\ u_y^m(i, 0) &= 0. \end{aligned} \quad (27)$$

The chemical potential  $\mu^m$  and the number density  $n^m$  on the bottom wall are calculated by

$$\begin{aligned} \mu^m(i, 0) &= [4\mu^m(i, 1) - \mu^m(i, 2)]/3, \\ n^m(i, 0) &= [4n^m(i, 1) - n^m(i, 2)]/3. \end{aligned} \quad (28)$$

With the updated macroscopic variables on boundary, the distribution function  $g_\alpha^m(i, 0)$  and  $f_\alpha^m(i, 0)$  are calculated by the NEM as follows

$$\begin{aligned} g_\alpha^m(i, 0) &= g_\alpha^{m,(eq)}(i, 0) + g_\alpha^m(i, 1) - g_\alpha^{m,(eq)}(i, 1), \\ f_\alpha^m(i, 0) &= f_\alpha^{m,(eq)}(i, 0) + f_\alpha^m(i, 1) - f_\alpha^{m,(eq)}(i, 1), \end{aligned} \quad (29)$$

where  $g_\alpha^{m,(eq)}$  and  $f_\alpha^{m,(eq)}$  are equilibrium distribution functions, which can be obtained from (8) and (14) with the updated macroscopic variables respectively. The implementation of the top wall is similar.

#### 4. Numerical simulations

In this section, we present several numerical examples to verify the lattice Boltzmann model for multiphase flows with variable density ratio and moving contact line. We implement the algorithm described in the previous sections based on PETSc [1]. The numerical tests are carried out on the Tianhe-2 supercomputer, which is ranked second of the Top-500 list as of June, 2017. The computing nodes of Tianhe-2 are comprised of two 12-core Intel Ivy Bridge Xeon CPUs with 64 GB local memory, and are interconnected via a proprietary high performance network. In the numerical experiments we use all 24 CPU cores in each node and assign one subdomain to each core.

##### 4.1. A bubble in the stationary flow

We first consider a benchmark test case: the 2D stationary bubble. In the simulation, a circular bubble is located at the center of a channel. The velocities of the top and bottom walls are set to be zero. The periodic boundary condition is employed at the direction  $x$ . The GNBC and the relaxation boundary condition are used in the top and bottom walls. The density ratio  $R_n = n_L/n_G$  and the dynamic viscosity ratio  $R_\eta = \eta_L/\eta_G$  both are set to be 1000. The other parameters are chosen as

$$\begin{aligned} n_L &= 1000, \quad n_G = 1, \quad \tau_n = 0.6, \quad \tau_\phi = 1.4, \\ \Gamma &= 400, \quad \Lambda = 0.01, \quad \beta = 100, \quad \xi = 7. \end{aligned} \quad (30)$$

For the 2D case, the Young–Laplace law is

$$\Delta p = \frac{\gamma}{R}, \quad (31)$$

where  $\Delta p$  is the pressure jump across the interface and  $R$  is the radius of the bubble. To check the Laplace law, we fix the mesh size as  $120 \times 120$ ,  $R = 30$  and investigate the pressure jump by changing the interfacial tension  $\gamma$ . In following of this paper, we usually set the mesh large enough such that the boundary effect can be ignored. It is well known that the discretization error decreases with the thickness of the interface layer increases [17]. We take an average value at mesh

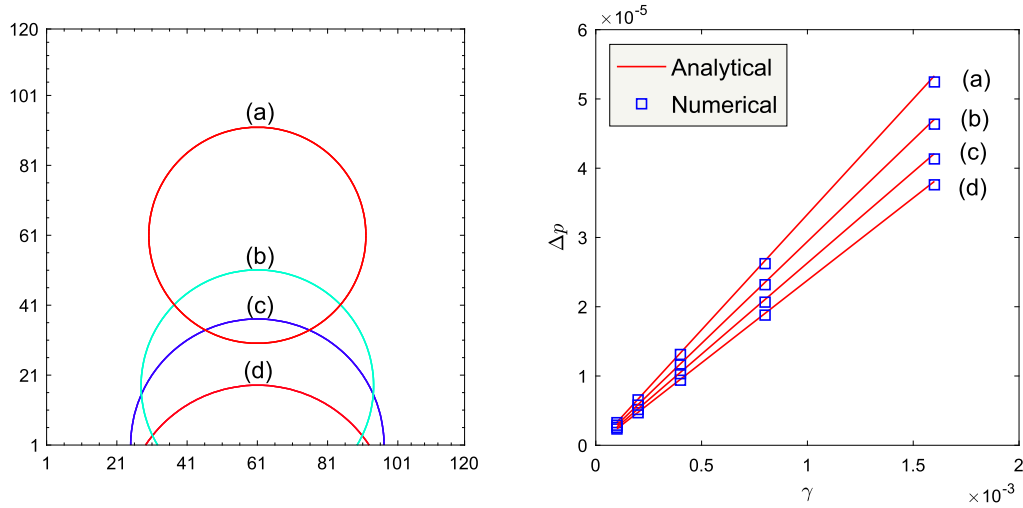


**Fig. 2.** The boundaries of the bubble or droplets at the initial step and the stopping step (left) and the verification of the Young–Laplace law (right). (a) Bubble in the center with  $R = 30$ . (b) Droplet contacts with the bottom wall with contact angle  $\theta^{\text{surf}} = 120^\circ$  and  $R = 34$ . (c) Droplet contacts with the bottom wall with contact angle  $\theta^{\text{surf}} = 90^\circ$  and  $R = 38$ . (d) Droplet contacts with the bottom wall with contact angle  $\theta^{\text{surf}} = 60^\circ$  and  $R = 42$ .

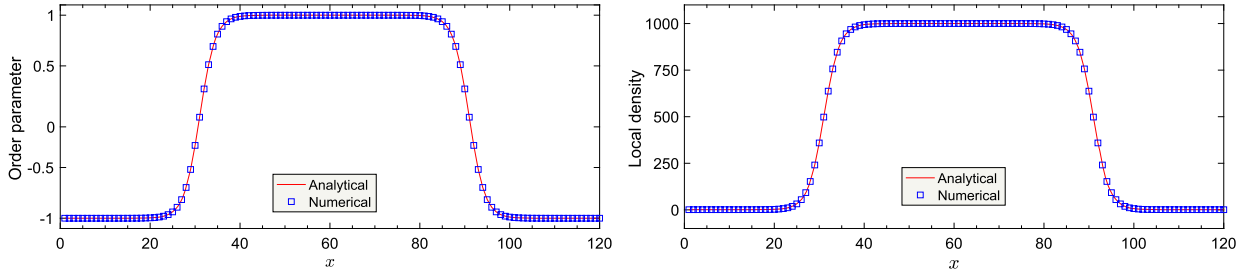


**Fig. 3.** The normalized order parameter  $\phi/\phi^*$  (left) and the local density  $n$  (right) in line  $y = 60$ .

points that are away from the interface of the bubble as the pressure inside or outside the bubble. The pressure jump, obtained from those average values, is plotted as a function of the interfacial tension in Fig. 2. It is observed that the numerical results match well with the analytical values from the Young–Laplace law, which verifies the Young–Laplace law. As mentioned in [12], the order parameter profile along the normal direction of the interface at the steady state is defined as

$$\phi = \phi^* \tanh\left(\frac{2(r - R)}{\xi}\right), \quad (32)$$

where  $r = \sqrt{(x - x_c)^2 + (y - y_c)^2}$  is the coordinate which is perpendicular to the interface,  $(x_c, y_c)^T$  are the coordinates of the center of the bubble. Fig. 3 shows the values of the order parameter and local density at line  $y = 60$ . It is clear that the numerical results obtained by the proposed method agree well with the analytical prediction. The case of the other directions is similar.

We are also interested in the verification of the Young–Laplace law in the case of the droplet contact with the wall. We fix the mesh size as  $120 \times 120$  and the thickness of the interface layer to be 7 as suggested by Fakhari and Rahimian [5]. The center of the droplet is respectively selected such that the initial contact angle equals to  $120^\circ$ ,  $90^\circ$ , and  $60^\circ$  with  $R = 34$ ,  $38$ , and  $42$ , respectively. In order to avoid the move of contact point, we set the static contact angle  $\theta^{\text{surf}}$  to be the same as the initial contact angle. The boundaries of the droplets at the initial step and the stopping step are shown in Fig. 2. Similar to the above simulation, we investigate the pressure jump by changing the interfacial tension  $\gamma$ . Fig. 2 displays the relationship between the pressure jump and the interfacial tension for the three different contact angles, which clearly shows the Young–Laplace law is also held in the case of the droplet contact with the wall.

#### 4.2. A droplet in contact with the wall

Next, we consider a droplet in contact with the wall and study the effect of the static contact angle, the density ratio, the slip coefficient, and the other phenomenological parameters. We fix the mesh size as  $120 \times 120$  in all simulations. The periodic boundary condition is employed at the  $x$  direction. The GNBC and the relaxation boundary condition are applied at

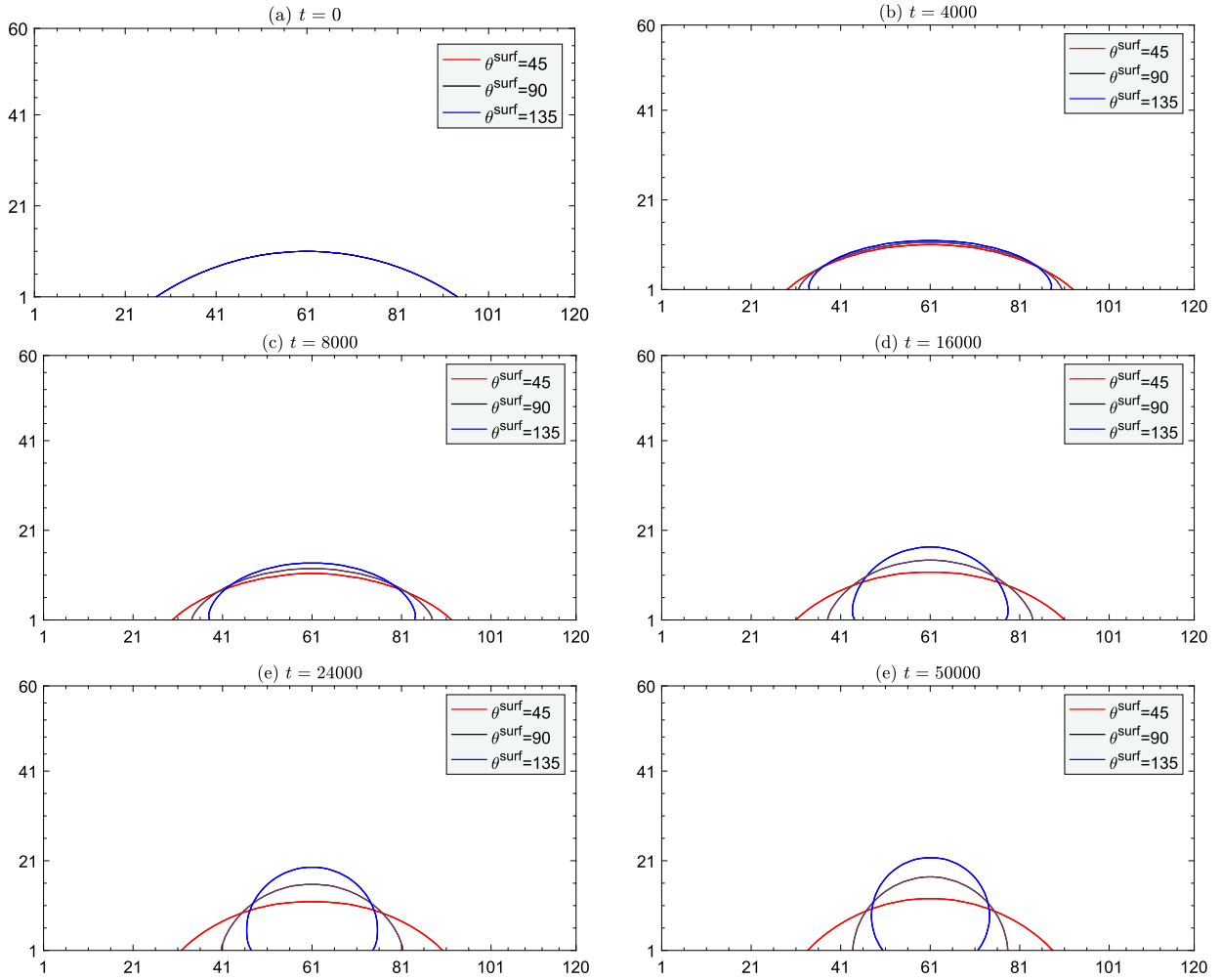


**Fig. 4.** Droplets in contact with the bottom wall with three different static contact angles which are  $\theta^{\text{surf}} = 45^\circ$ ,  $90^\circ$ , and  $135^\circ$ , respectively. The surfaces of the droplet at different time steps.

the top and bottom walls. In this case, the top and bottom walls are fixed. The density ratio and the dynamic viscosity ratio are chosen as  $R_n = 100$  and  $R_\eta = 10$ , respectively. The other parameters are chosen as

$$\begin{aligned} n_L = 100, \quad n_G = 1, \quad \gamma = 0.2, \quad \eta_L = 1, \quad \tau_\phi = 1.5, \\ \Gamma = 200, \quad \xi = 2.8, \quad \Lambda = 0.01, \quad \beta = 30. \end{aligned} \quad (33)$$

The interface is initialized using the following profile in the direction normal to the interface

$$\phi = \phi^* \tanh\left(\frac{2(r - R)}{\xi}\right). \quad (34)$$

We first simulate three test cases with different static contact angles which are  $\theta^{\text{surf}} = 45^\circ$ ,  $90^\circ$ , and  $135^\circ$ , respectively. The other parameters in the lattice Boltzmann model are given in equation (33). In the simulations, a circular droplet with radius  $R = 60$  is in contact with the bottom wall with a contact angle  $33.56^\circ$  initially (see Fig. 4-(a)). The center of the droplet is located at  $(60, -50)$ . Since the static contact angle is larger than the initial contact angle, the droplet retracts as time evolution. The surfaces of the droplets at  $t = 0, 4000, 8000, 16000, 24000, 50000$  are displayed in Fig. 4. It is clear that the contact point moves fast with the increase of the static contact angle.

We then run the test cases with different density ratios, which are  $R_n = 100, 200, 400$ . The dynamic viscosity ratio is fixed to be  $R_\eta = 10$ . In all simulations, the density of the fluid, the interface tension, the steady state contact angle, and the mobility parameter are respectively set as  $n_L = 100$ ,  $\gamma = 0.2$ ,  $\theta^{\text{surf}} = 60^\circ$ ,  $\tau_\phi = 3.5$ ,  $\Gamma = 200$ ,  $\Lambda = 0.1$  and  $\beta = 50$ . The initial state is given in Fig. 4-(a). The surfaces of the droplets at different time steps are shown in Fig. 5. It is clear that the dynamics of the droplets with different density ratios are similar.



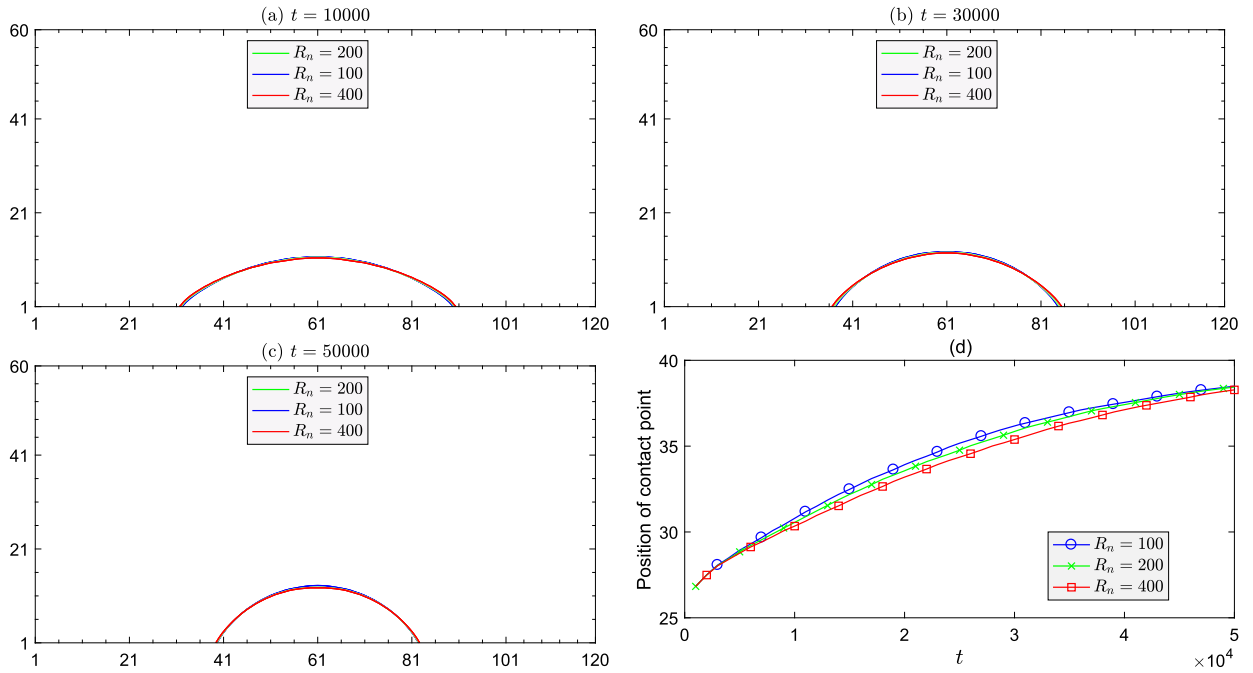


**Fig. 5.** Droplets in contact with the bottom wall with three different density ratios  $R_n = 100$ , 200, and 400. The surfaces of the droplet at different time steps and the histories of the position of the contact point.

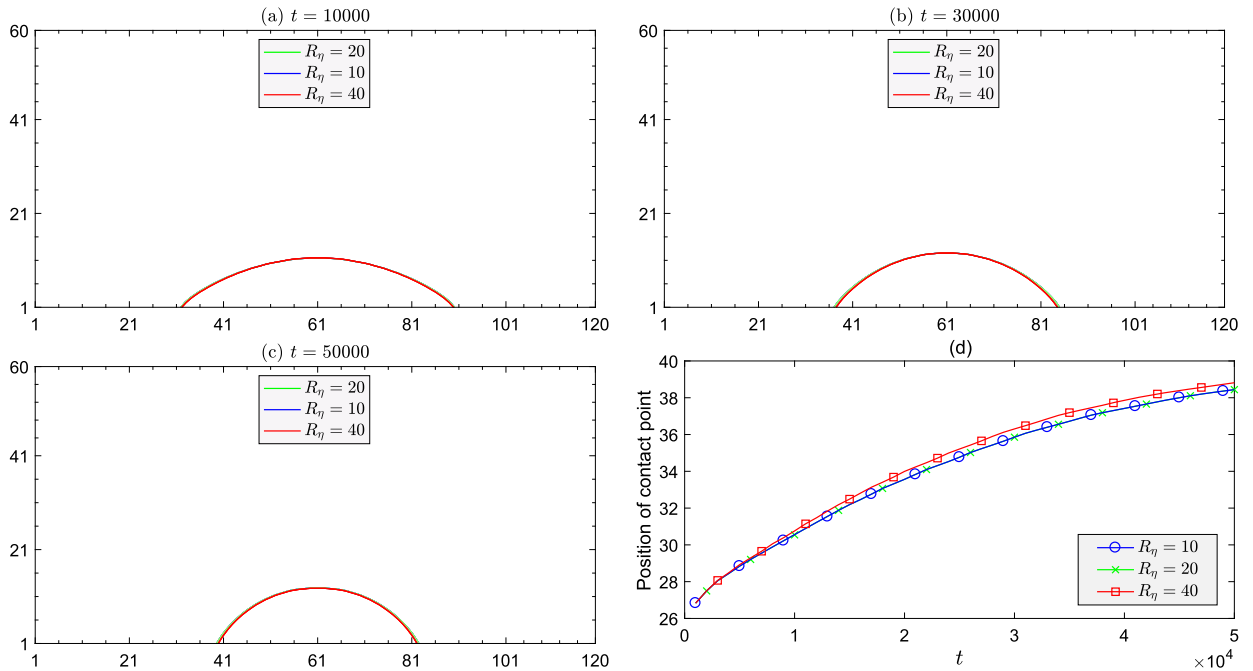


**Fig. 6.** Droplets in contact with the bottom wall with three different dynamic viscosity ratios  $R_\eta = 10$ , 20, and 40. The surfaces of the droplet at different time steps and the histories of the position of the contact point.

Next, we set the density ratio as  $R_n = 200$  and run the simulations with different dynamic viscosity ratios, which are  $R_\eta = 10$ , 20 and 40, respectively. The interfaces of the droplets at different time steps are plotted in Fig. 6, which shows the simulations with different dynamic viscosity ratios are also similar.

Next, we study the effect of the slip coefficient and interfacial tension during the droplet retracting process. The gas density and the dynamic viscosity ratio are set as  $n_G = 50$  and  $R_\eta = 2$ . The mobility parameters  $\Gamma$  and  $\Lambda$  are 50 and 1,

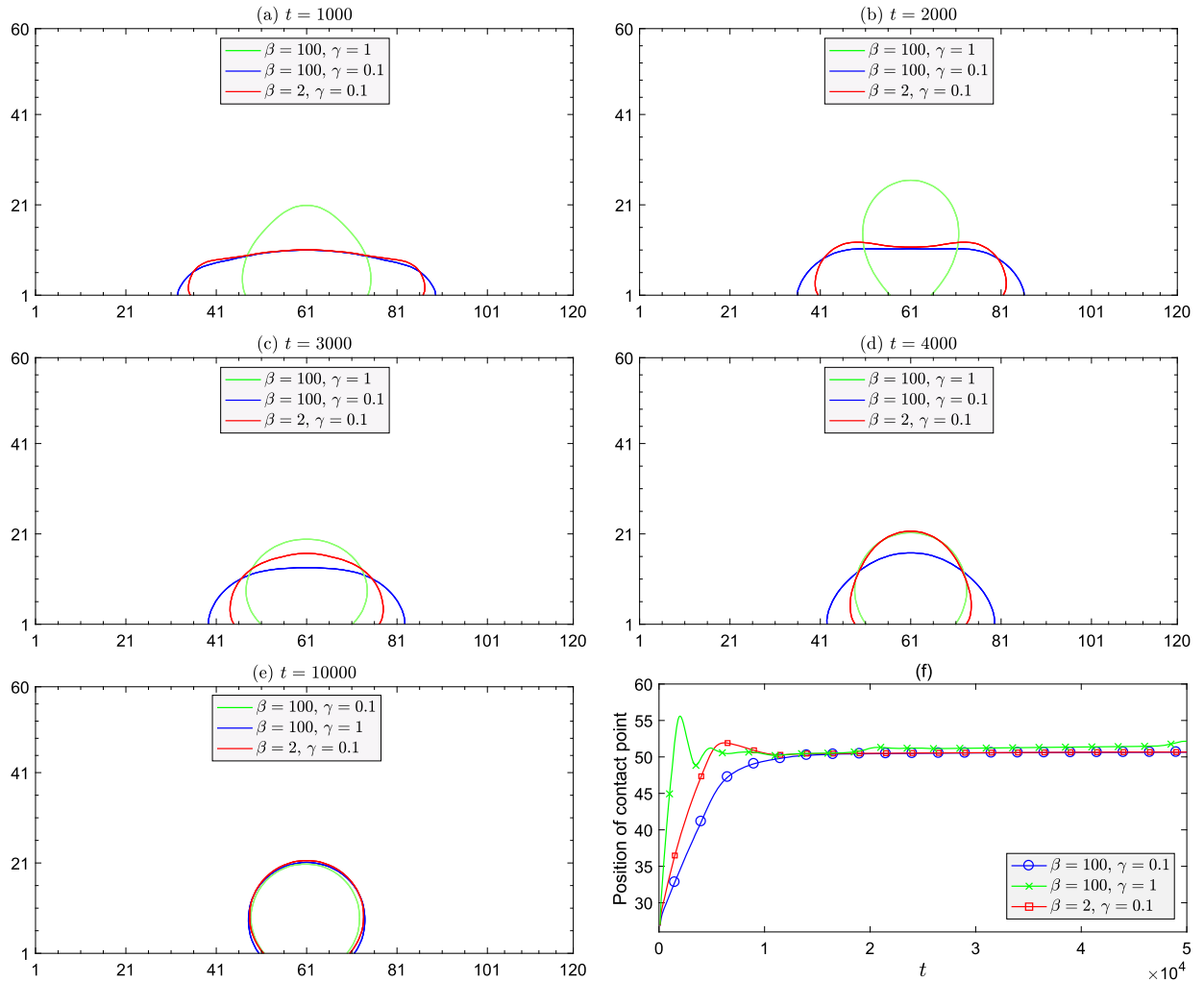


**Fig. 7.** Droplets in contact with the bottom wall. The boundaries of the droplet for the three test cases, which are case 1:  $\beta = 100$ ,  $\gamma = 0.1$ , case 2:  $\beta = 100$ ,  $\gamma = 1$ , and case 3:  $\beta = 2$ ,  $\gamma = 0.1$ , at different time steps and the histories of the position of the contact point.

respectively. The static contact angle  $\theta^{\text{surf}}$  is set to be  $135^\circ$ . The initial state is shown in Fig. 4-(a). The other parameters are unchanged. For comparison, we consider three test cases with different slip coefficients and surface tensions, which are case 1:  $\beta = 100$ ,  $\gamma = 0.1$ , case 2:  $\beta = 100$ ,  $\gamma = 1$ , and case 3:  $\beta = 2$ ,  $\gamma = 0.1$ , respectively. The boundaries of the droplets at different time steps and the histories of the position of the contact point are shown in Fig. 7. For the case with large surface tension and small slip coefficient, the droplet initially starts to retract quickly due to surface tension, then it spreads due to flow inertial and the contact point reaches a maximum distance. The process then repeats and contact point oscillate around  $x = 50.66$  and eventually reaches the steady state position with a contact angle equal to the static contact angle  $\theta^{\text{surf}} = 135^\circ$ . From Fig. 7-(f), we observe that the contact point moves slowly with the interfacial tension decreases or the slip coefficient increases.

#### 4.3. Droplet rising under buoyancy

In this subsection, we consider a two-dimensional droplet rising under buoyancy. The single droplet in quiescent liquid is surrounded with stationary walls. The gravitational effects can be applied to the entire fluid by incorporating the body force  $(n - n_L)\mathbf{g}$  everywhere. We choose the parameters as follows

$$\begin{aligned} n_L = 1.42, \quad n_G = 0.58, \quad \gamma = 0.0052, \quad \tau_n = 0.875, \quad \tau_\phi = 1, \\ \Gamma = 2, \quad \xi = 2.8, \quad \Lambda = 0.1, \quad \beta = 200. \end{aligned} \quad (35)$$

The computational domain is set to be  $80 \times 300$ . The center of the droplet is initially located at  $40 \times 75$  with the radius of  $R = 10$ . The dimensionless parameters (Archimedes, Eötvös, and Morton number) are defined as [32]

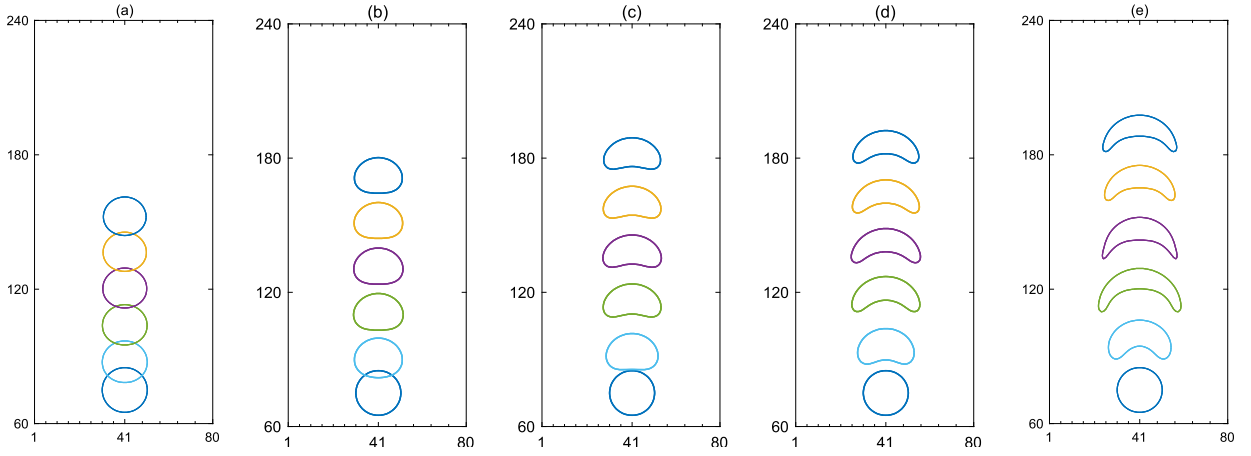


**Fig. 8.** Droplet rising under buoyancy with density ratio  $n_L/n_G = 2.45$ . The interfaces of the droplets at  $t^* = 0, 4, 8, 12, 16, 20$  (from bottom to up) in different test cases are plotted. (a)  $Eo = 5$ ,  $Mo = 0.2267$ ; (b)  $Eo = 10$ ,  $Mo = 0.4535$ ; (c)  $Eo = 20$ ,  $Mo = 0.907$ ; (d)  $Eo = 40$ ,  $Mo = 1.8134$ ; (e)  $Eo = 100$ ,  $Mo = 4.535$ .

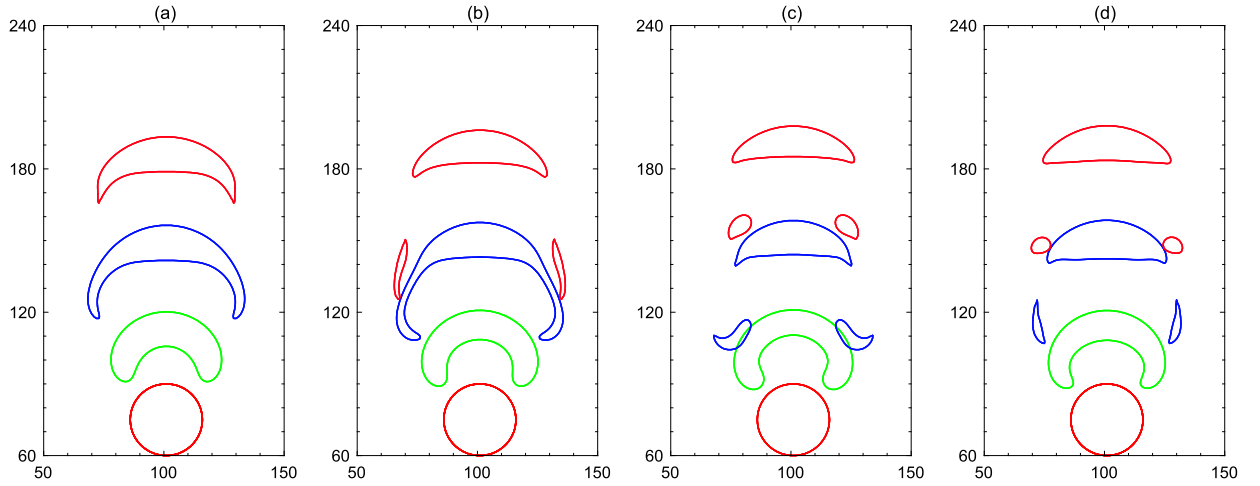


**Fig. 9.** Droplet rising under buoyancy with density ratio  $n_L/n_G = 5$ . The interfaces of the droplets at  $t^* = 0, 3, 6, 9$  (from bottom to up) in different test cases are plotted. (a)  $Ar = 45$ ,  $Eo = 86.4$ , and  $Mo = 0.246$ ; (b)  $Ar = 90$ ,  $Eo = 86.4$ , and  $Mo = 0.0154$ ; (c)  $Ar = 180$ ,  $Eo = 86.4$ , and  $Mo = 9.6e-4$ ; (d)  $Ar = 180$ ,  $Eo = 43.2$ , and  $Mo = 1.20e-4$ .

$$Ar = \frac{n_L \sqrt{8|\mathbf{g}|R^3}}{\eta_L}, \quad Eo = \frac{|\mathbf{g}|(n_L - n_G)(2R)^2}{\gamma}, \quad Mo = \frac{|\mathbf{g}|(n_L - n_G)\eta_L^4}{n_L^2 \gamma^3}, \quad (36)$$

where  $\mathbf{g}$  is the gravity. We take five test cases with the Eötvös number  $Eo$  increasing from 5 to 100 and the Morton number increasing from 0.2267 to 4.535, which are the same as those used by [32]. The non-dimensional time  $t^*$  is defined as  $t^* = \frac{t}{\sqrt{2R/|\mathbf{g}|}}$ . The interfaces of the droplet in the five test cases are shown in Fig. 8. As  $Eo$  increases, the shape of the droplet deforms more and more from Fig. 8-(a) to Fig. 8-(e). The results of the new proposed method are very similar to those of Takada's method [32].

Next, we study the breakup of an axisymmetric bubble at high Archimedes number. Some parameters are reset as

$$n_L = 5, \quad n_G = 1, \quad \gamma = 0.01, \quad \tau_\phi = 1, \quad \Gamma = 2, \quad \xi = 2.8. \quad (37)$$

The computational domain is set as  $200 \times 300$ . The droplet with radius  $R = 15$  is located at  $(100, 75)$ . The Eötvös number is fixed as 86.4. Three different Archimedes numbers  $Ar = 45, 90$ , and  $180$  ( $Mo = 0.246, 0.0154$ , and  $9.6e-4$ ) are considered. The history of the interface of the droplet is displayed in Fig. 9. It is clearly shown that the droplet rapidly evolves into a torus bubble and then breaks up as high Archimedes number is used. For comparison, we also run a case with parameters  $Ar = 180$ ,  $Eo = 43.2$ , and  $Mo = 1.20e-4$ . As shown in Fig. 9, the results with the same Archimedes number and two different Eötvös numbers are very similar.

#### 4.4. Droplet splash on a wall or liquid film

In the subsection, a droplet splash on a wall or liquid film is considered, which is fundamental in various applications [36]. The important relevant non-dimensional parameters are the Weber number ( $We = 2n_L U^2 R / \gamma$ ) and the Reynolds number ( $Re = 2n_L U R / \eta_L$ ) [17]. In the dimensionless numbers,  $R$  is the initial droplet radius,  $n_L$  is the liquid density, and  $U$  is the initial impact velocity. We first simulate a droplet splash on a liquid film, which is also studied in [17,19,29]. The total computational domain is set to be  $1200 \times 400$ . Initially, a liquid layer with height of 40 is on the bottom wall and a droplet with radius  $R = 100$  is located at the position (600, 140) in the computational domain. The initial impact velocity is set as  $U = 0.05$ . The simulation parameters are set as  $n_L = 5$ ,  $n_G = 1$ ,  $\xi = 5$ ,  $\tau_\phi = 1$ , and  $\Gamma = 90$ . The non-dimensional time  $t^*$  is defined as  $t^* = \frac{Ut}{2R}$ .

The Weber number is fixed at  $We = 5000$ , while the Reynolds number is changed from 50 to 1000 by tuning the viscosity. The results are shown in Fig. 10. In each frame, the findings for the current MRT lattice Boltzmann model with GNBC are given on the right, while the results for the MRT lattice Boltzmann model with no-slip boundary condition are plotted on the left. Since the fluid–gas interface is out of touch with the solid wall, the outcomes of the two method should be similar, which is verified by the numerical results. We also notice that the deformation rate increases as the Reynolds number becomes large. Moreover, the influence of the density ratio is also studied. The Weber number and the Reynolds number are fixed as 5000 and 200, respectively. Cases with density ratios of 5, 10, 20, and 50 are simulated and the results at  $t^* = 1$  are given in Fig. 11. As the density ratio is increased to 50, a liquid sheet coming out of the neck is observed. However, we are unable to do a simulation based on the current model with the density ratio larger than 100. For this case with large density ratio, one can follow the models given in [19,18,22,29,34,35].

Now, we consider a droplet splash on the solid wall, which is also studied in [24] by MRT lattice Boltzmann model together with a contact angle model. For the reason of comparison, the droplet with  $R = 50$  is located at the position (300, 50). The initial impact velocity is set as  $U = 0.01$ . The total computational domain is set to be  $600 \times 200$ . The simulation parameters are set as  $n_L = 5$ ,  $n_G = 1$ ,  $\xi = 5$ ,  $\tau_\phi = 0.6$ ,  $\Lambda = 100$ ,  $\beta = 0.1$ ,  $\theta^{\text{surf}} = 87.4^\circ$ , and  $\Gamma = 100$ ,  $Re = 150$ . The Weber numbers for three simulations are  $We = 30, 75$ , and  $137$ . The evolutions of the droplet in the three simulations are presented in Fig. 12. Immediately after the droplet coming in contact with the solid wall, the shape of the droplet becomes a cut sphere. At  $t^* = 0.6$ , the droplet causes radial outward flow of liquid resulting in the formation of a lamella. Then the lamella continues to grow radially and its thickness decreases. After reaching a maximum spread, the lamella starts recoiling due to surface tension force. The droplet reaches the equilibrium state finally, after a couple of oscillations involving spread and recoil. The spread and recoil behavior of our numerical simulation is similar with the experiment reported by Kim and Chun [15]. The evolution of the spread factor  $R^*$  is given in Fig. 13, in which the spread factor  $R^*$  is defined as  $R^* = \frac{R(t)}{R}$ . Here  $R(t)$  is the spreading radius of the droplet on the solid wall. From Fig. 13, we observe that the oscillation amplitude increases as the Weber number increasing.

#### 4.5. Two stationary droplets on the wall

The fifth test case, we consider two stationary droplets on the wall without collision. The periodic boundary condition is employed at the direction  $x$ . The GNBC and the relaxation boundary condition are used in the top and bottom walls. The top and bottom walls are fixed at all time steps. The two stationary droplets are located at the bottom wall with the same initial contact angle. The gap of the two droplets ( $d$ ) is set to be 5. The parameters are chosen as

$$\begin{aligned} n_L = 100, \quad n_G = 10, \quad \tau_n = 0.505, \quad \tau_\phi = 0.6, \quad \gamma = 0.4, \\ \Gamma = 400, \quad \Lambda = 0.1, \quad \beta = 3, \quad R_\eta = 10, \quad \theta^{\text{surf}} = 90^\circ. \end{aligned} \quad (38)$$

It is easy to understand that the gap between the bubbles and the interface thickness are the major factors to decide whether the two stationary droplets will merge or not. We first run two simulations with the interface thickness  $\xi = 2.4$  or  $\xi = 2.6$ . The gap of the two droplets is larger than  $2\xi$  for  $\xi = 2.4$  and is smaller than  $2\xi$  for  $\xi = 2.6$ . The mesh size is also set as  $120 \times 120$  in the simulations. The two stationary droplets have the same radius  $R = 20$  and center at (38, 0) and (83, 0), respectively (see Fig. 14-(a)). The initial contact angles for the two droplets are set to be  $90^\circ$ . As shown in Fig. 14, the two droplets do not merge when  $\xi = 2.4$ , but will merge eventually for  $\xi = 2.6$ . Fig. 14-(h) shows the history of the position of the contact point for  $\xi = 2.6$ . It is observed that oscillation occurs during the merging process. To check the reason of this phenomenon, we do three simulations for contrast, which are denoted as “Case 1”, “Case 2”, and “Case 3”. In “Case 1”,  $\tau_\phi$  is set to be 1.6 and the other parameters are unchanged; in “Case 2”,  $\Lambda$  is set to be 1 with the other parameters unchanged; in “Case 3”,  $\beta$  is set to be 3 with the other parameters unchanged. The numerical results show that the oscillation disappears with a large  $\beta$  used. We also conclude that the oscillation amplitude is effected by the phenomenological parameter  $\Lambda$  and the relaxation time  $\tau_\phi$ .

Next, we set  $\tau_\phi = 4.6$ ,  $\xi = 2.6$ ,  $\Lambda = 0.1$ ,  $\gamma = 0.4$ , and  $\beta = 10$ , to study the effect of the static contact angle  $\theta^{\text{surf}}$  in the merging process. The mesh size is also set as  $200 \times 150$  in the simulations. The two stationary droplets located at the bottom wall which center at (68, 15) and (133, 15) with the same radius  $R = 30$  (see Fig. 15-(a)). The two droplets also have the same initial contact angle ( $120^\circ$ ). It is important to noting that the gap of the two droplets is smaller than  $2\xi$ . We consider three different static contact angles which are  $\theta^{\text{surf}} = 90^\circ, 120^\circ$ , and  $135^\circ$ , respectively. The boundaries of the two

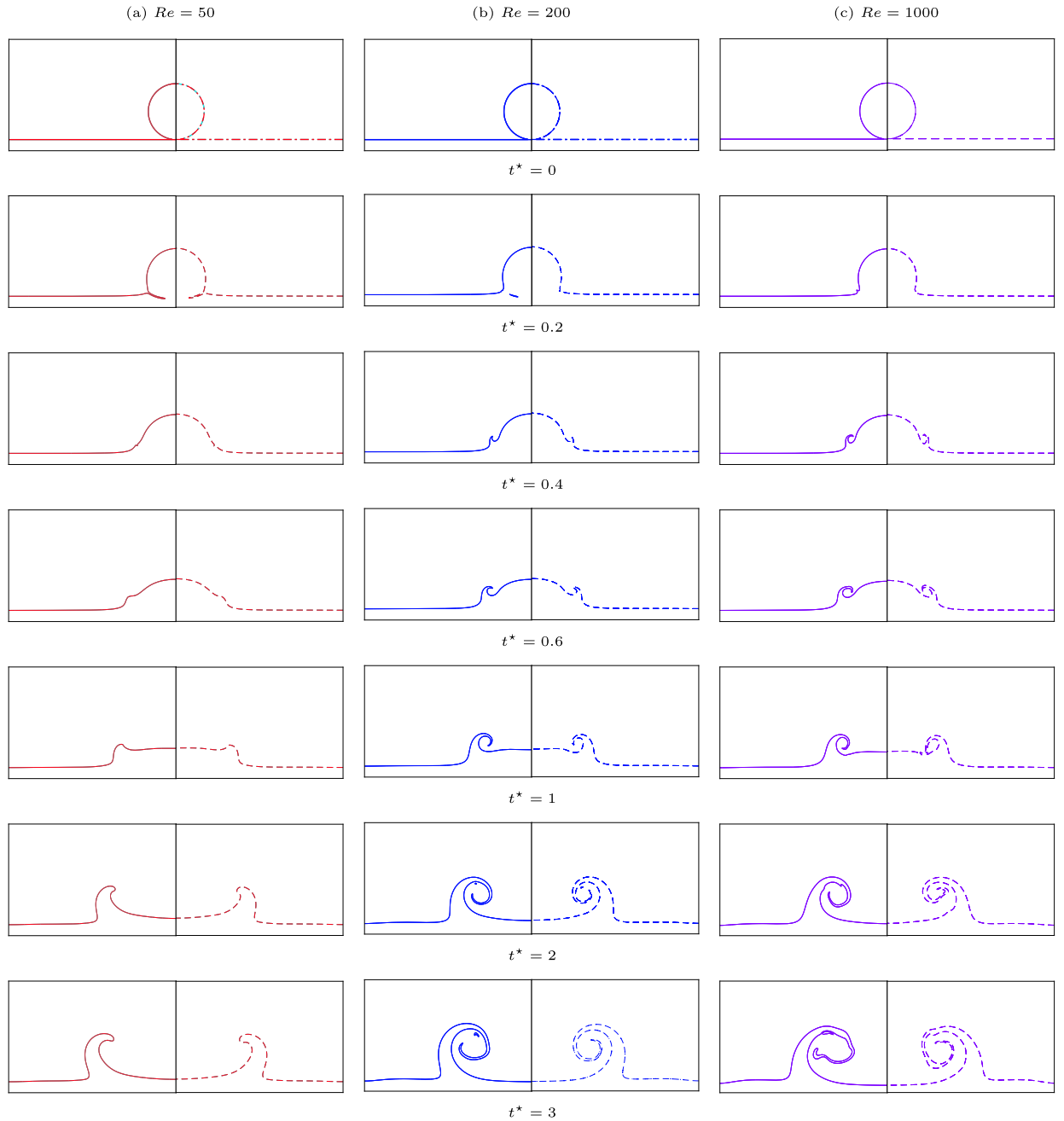


**Fig. 10.** Droplet splashing on a wet surface. Left:  $Re = 50$ , middle:  $Re = 200$ , right:  $Re = 1000$ . In each column, the left frames (solid line) represent the MRT lattice Boltzmann model with no-slip boundary condition and the frames on the right (dash dot line) are for the MRT lattice Boltzmann model with GNBC.

droplets at different time steps are given in Fig. 15. For the case with the static contact angle  $\theta^{\text{surf}} = 90^\circ$ , the two droplets start to retract due to surface tension during the time interval (0, 10000) and then merge together. The distribution of the order parameter  $\phi$  at the steady state for the simulation is shown in Fig. 15-(f), which clearly verifies that a perfect droplet is obtained. For the case with the static contact angle  $\theta^{\text{surf}} = 120^\circ$ , the contact points are motionless until the two droplets merge. After long time evolution, a steady state as shown in Fig. 15-(g) is obtained. From Fig. 15-(g), we observe that the contact angle at the steady state matches well with the given steady state contact angle. The numerical result also shows that there is a small liquid droplet inside the gas droplet with a contact angle equals  $\theta^{\text{surf}}$  equals to  $60^\circ$ . We also note that the steady state contact angle of the liquid plus the steady state contact angle of the gas equals to  $180^\circ$ . For the case with static contact angle  $\theta^{\text{surf}} = 135^\circ$ , the two droplets spread until the static contact angle reached in the time interval

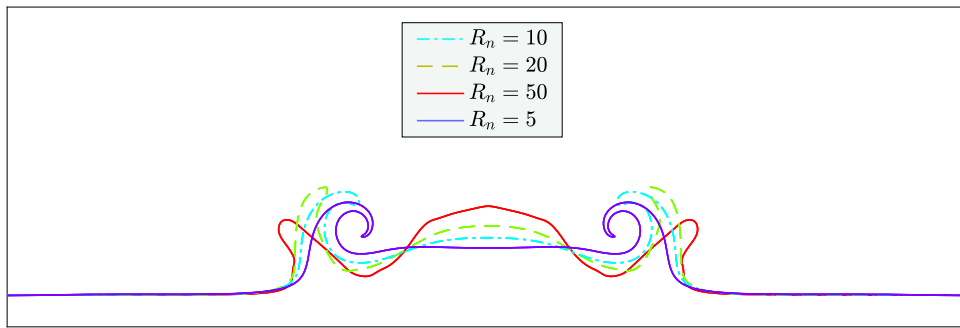


**Fig. 11.** Droplet splashing on a wet surface with different density ratios.  $Re = 100$ ,  $We = 5000$ .



**Fig. 12.** Droplet splashing on solid wall. Left:  $We = 30$ , middle:  $We = 75$ , right:  $We = 137$ .

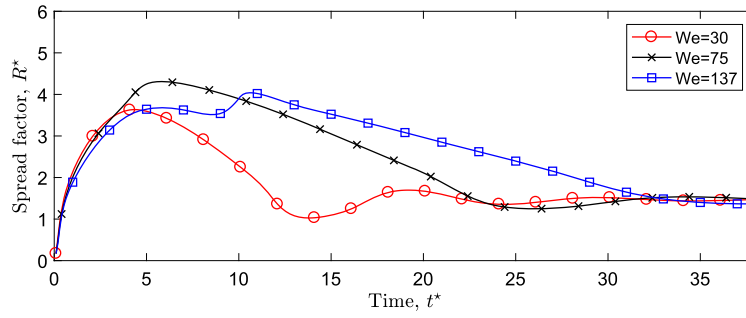


**Fig. 13.** Droplet splashing on solid wall, spread factor evolution with different Weber numbers.

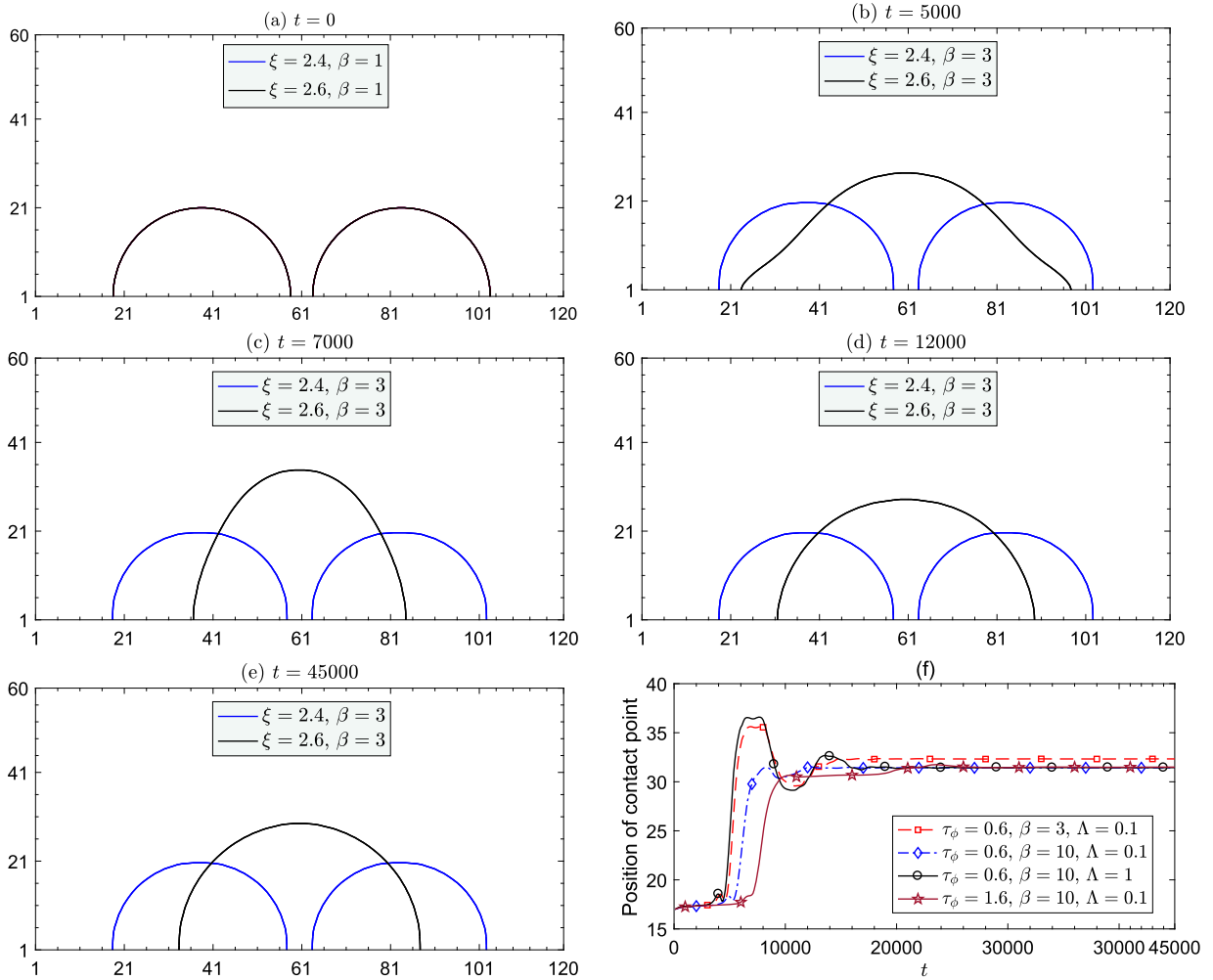


**Fig. 14.** Two stationary droplets on the wall. The boundaries of the droplets at different time steps (a)–(e) and the histories of the position of the contact point (f).

(0, 7000). The two droplets then merge together. The steady state of the contact angle is shown in Fig. 15-(h). Similar to the case with  $\theta^{\text{surf}} = 120^\circ$ , there is also a small liquid droplet inside the gas droplet with a contact angle equals  $\theta^{\text{surf}}$  equals to  $45^\circ$ .

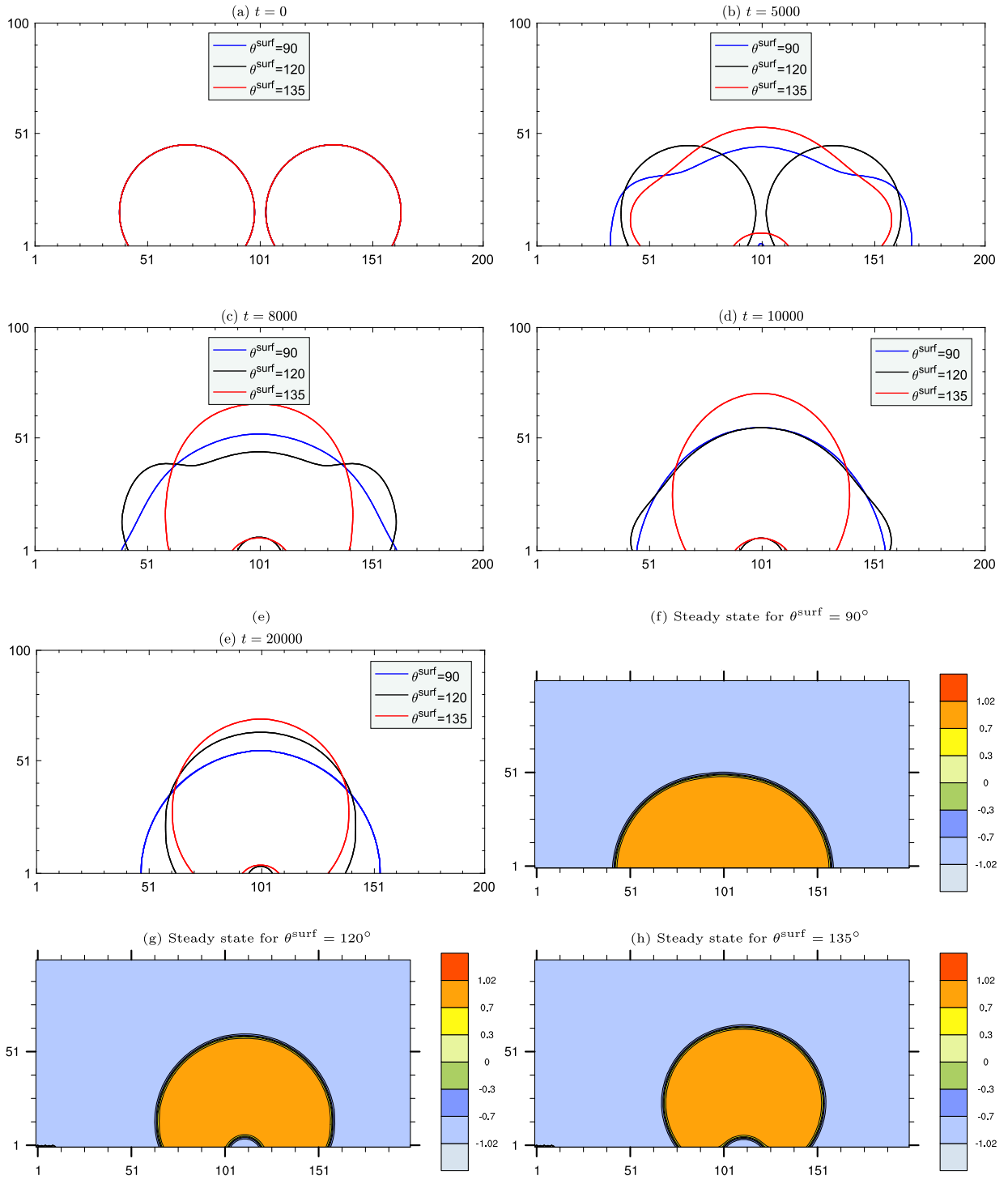


**Fig. 15.** Two stationary droplets on the wall. The boundaries of the two droplets contact with the bottom wall.  $\theta^{\text{surf}} = 90^\circ$ ,  $120^\circ$ , and  $135^\circ$ . Note that, the order parameter is normalized by  $\phi^*$  for visualization.

#### 4.6. Two phase Couette flow

In this test, we simulate the Couette flow with the top and bottom walls moving with velocity  $u_w = 0.0001 \times (1 - e^{-t/20000})$  in opposite directions. The GNBC and the relaxation boundary condition are used at the top and bottom walls



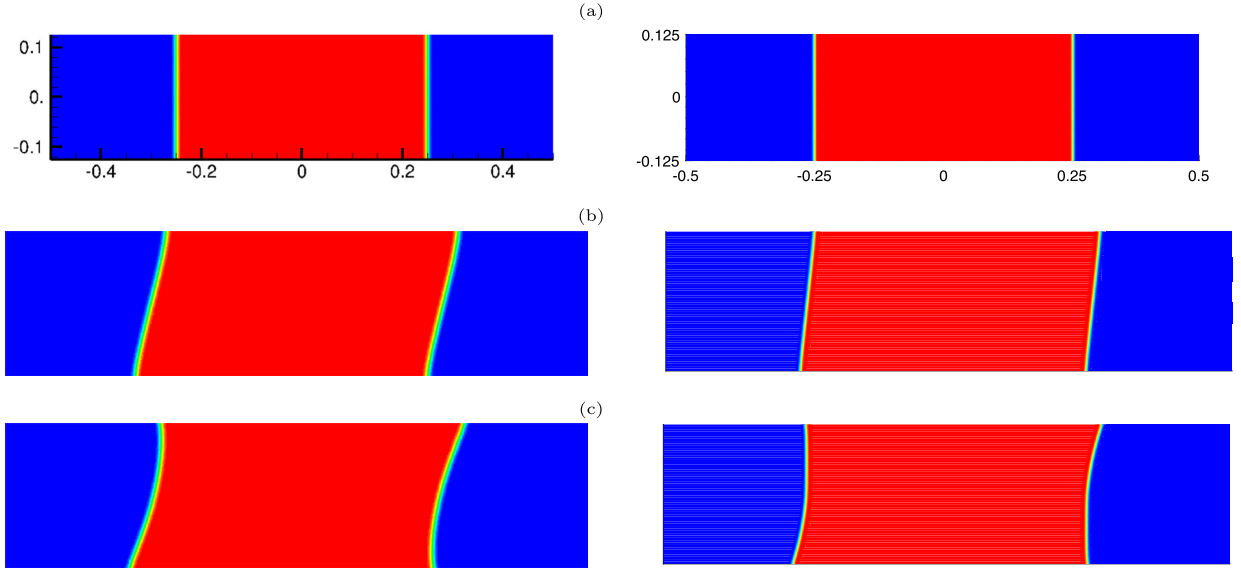


**Fig. 16.** The distributions of the order parameter for Couette flow. In each row, the figure in the left represents the results of Navier–Stokes model, and the plot in the right denotes the outcomes of the of the lattice Boltzmann model. The results of Navier–Stokes model are taken from [2]. (a) Initial state for the two cases; (b) the interface structure for the symmetric case at time of 1.875; (c) the interface structure for the asymmetric case at time of 1.875.

while periodic boundary conditions are used at left and right boundaries. The mesh size is fixed as  $240 \times 60$  in all simulations. The parameters are chosen as

$$\begin{aligned} n_L = 2.2, \quad n_G = 0.2, \quad \tau_n = 0.53, \quad \tau_\phi = 2.6, \quad \gamma = 0.0003, \\ \Gamma = 10, \quad \Lambda = 1.316, \quad \beta = 0.088, \quad \xi = 2.715. \end{aligned} \quad (39)$$

The initial condition of  $\phi$  is shown in Fig. 16-(a) and the final time is set to be 900 000 in lattice units. The computational domain is  $[-120, 120] \times [-30, 30]$  in lattice units. The two interfaces of the initial state are located at  $x = -60$  and  $x = 60$ , respectively. After scaling the length by  $L = 240$ ,  $\phi$  by  $\phi^* = 1$ , velocity by  $V = 0.0005$ , time by  $L/V = 480\,000$ , number density by  $n = 2.2$ , viscosity by  $\eta = 0.053$  and pressure by  $\eta V/L = 2.2 \times 10^{-7}$ , we get the normalized parameters in the simulation as follows

$$\mathcal{R} = 5, \quad l_s = 0.0025, \quad \epsilon = 0.004, \quad \mathcal{B} = 12, \quad \mathcal{V}_s = 200, \quad \mathcal{L}_d = 5 \times 10^{-5}.$$

Compare with the first test case in [2], the parameters are the same except that we use a smaller  $\mathcal{L}_d$  for better stability in our method. Since  $\mathcal{L}_d$  is a parameter which controls the phenomenological mobility, the steady state of the two models should be the same. The normalized final time is 1.875. More details about normalization are given in Appendix A. In the simulation, two experiments with the different static contact angles  $77.6^\circ$  (asymmetric case) and  $90^\circ$  (symmetric case) are conducted respectively. The interfaces for the two cases in the steady state are shown in Fig. 16. The velocity field and streamlines for the asymmetric case at  $t = 1.875$  are shown in Fig. 17. In Fig. 16 and Fig. 17, we take the numerical results of the Navier–Stokes model and lattice Boltzmann model together for comparison. The distributions of the order parameter and the velocity compare well with the results obtained by solving the coupled Navier–Stokes equations and Cahn–Hilliard equation with finite element method [2]. The velocity  $u_x$  along lower boundary is plotted in Fig. 18, which shows large slipping around the contact point.

To study the strong parallel scalability, a test on a  $3000 \times 3000$  mesh is considered. The simulation is stopped at  $t = 2000$ . Fig. 19 shows the total compute time and the speedup with respect to the number of processors. We see that the compute time of the proposed method decreases with the number of processors increases. An almost ideal speedup is obtained from 196 to 3072 processors. Due to the efficiency and good strong scalability of the proposed method, the method could be greatly improved, especially for 3D applications.

## 5. Concluding remarks

In this paper, a lattice Boltzmann model for multiphase flows with variable density ratio and moving contact line is studied. To improve numerical stability, a semi-implicit lattice Boltzmann method together with a mixed finite difference scheme is proposed. The GNBC and the relaxation boundary condition are implemented to describe the behavior of the droplet on the boundary. With the updated boundary macroscopic variables, the density distribution functions on the boundary are obtained by the NEM. Some typical numerical tests are successfully carried out to verify the proposed model. The behavior

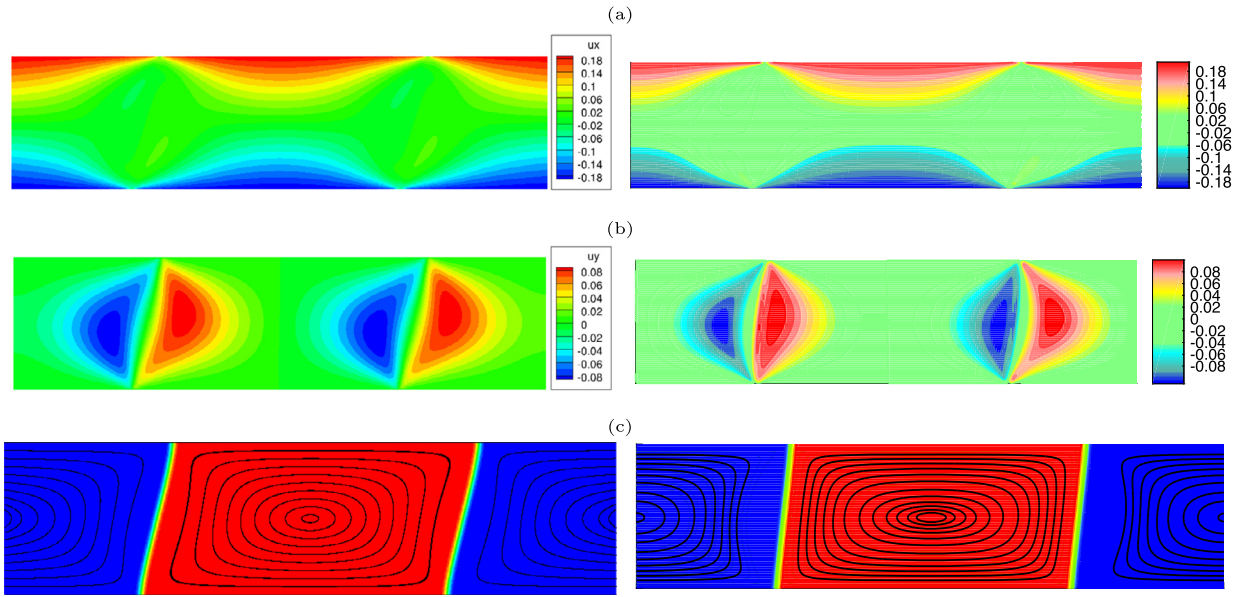


**Fig. 17.** The velocity field in x direction (a), in y direction (b), and the streamline (c) for symmetric case at time of 1.875. In each row, the figure in the left represents the results of Navier–Stokes model, and the plot in the right denotes the outcomes of the of the lattice Boltzmann model. The results of Navier–Stokes model are taken from [2].

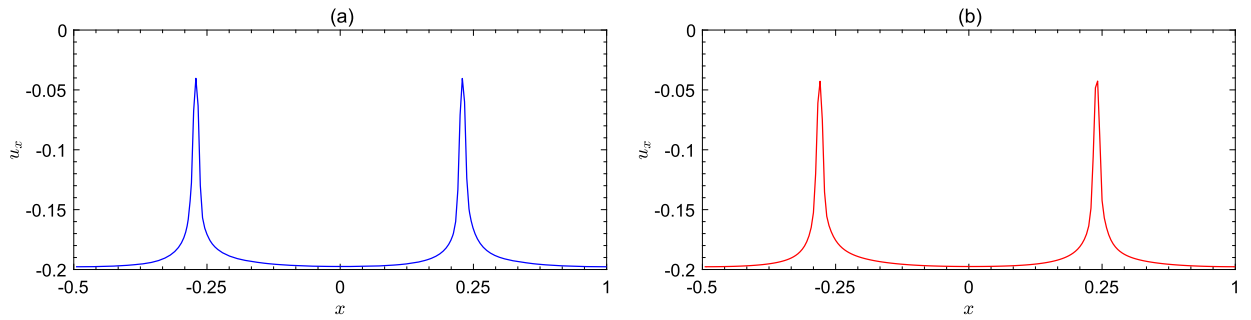


**Fig. 18.** The velocity profiles on the bottom boundary for the symmetric case (a) and asymmetric case (b) at time of 1.875. Note that, the velocity is normalized by  $V = 0.0005$  for visualization.

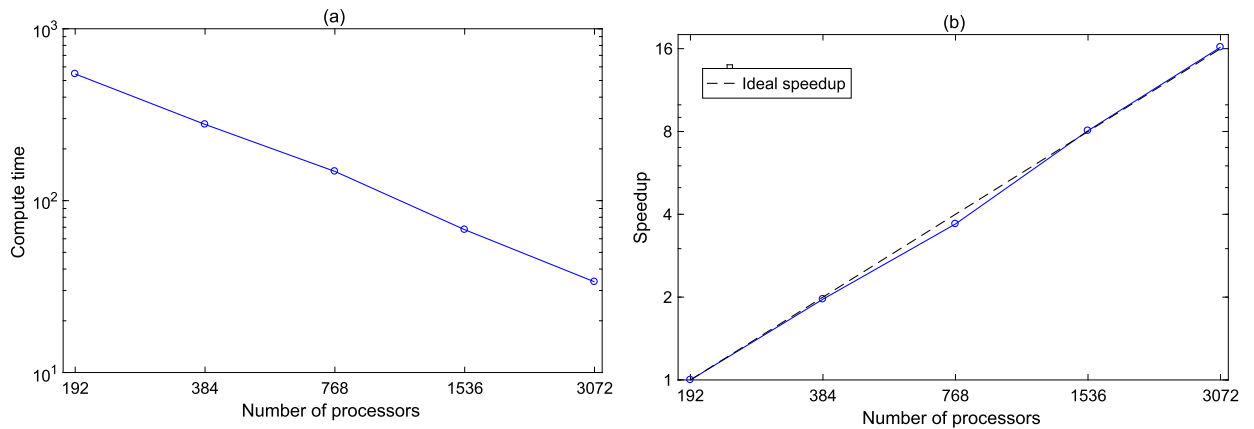


**Fig. 19.** Strong scaling results for solving the Couette flow.  $3000 \times 3000$  mesh, 2000 time steps.

of the solution near the contact line is examined. The efficiency and good strong scalability of the proposed method show the potential application in 3D.

### Acknowledgements

This publication was supported in part by the Hong Kong RGC-GRF grants 16302715 and 16324416, and Hong Kong RGC-CRF grant C6004-14G, and NSFC 11501554. We would like to express our appreciation to the anonymous referees for their invaluable comments, which have greatly improved the quality of the paper.

### Appendix A. Normalization

Let us conclude the recovered Cahn–Hilliard equation and Navier–Stokes equations from the lattice Boltzmann model as

$$\begin{cases} \frac{\partial \phi}{\partial t} + \nabla \cdot (\phi \mathbf{u}) - \theta_M \nabla^2 \mu = 0, \\ \nabla \cdot \mathbf{u} = 0, \\ n \frac{\partial \mathbf{u}}{\partial t} + n \nabla \cdot (\mathbf{u} \cdot \mathbf{u}) = -\nabla p + \eta \nabla^2 \mathbf{u} + \mathbf{G}_{\text{ext}} + \mu \nabla \phi, \end{cases} \quad (40)$$

together with  $\mu = -\kappa \nabla^2 \phi + 4A[\phi^3 - (\phi^*)^2 \phi]$  and the following boundary conditions

$$\beta u_x^{\text{slip}} = -\eta \partial_{\mathbf{n}} u_x + L(\phi) \partial_x \phi / \phi^*, \quad (41)$$

$$\frac{\partial \phi}{\partial t} + u_x \partial_x \phi = -\Lambda L(\phi), \quad (42)$$

$$u_y = 0, \quad \partial_{\mathbf{n}} \mu = 0. \quad (43)$$

Here parameters  $\theta_M$ ,  $\kappa$  and  $A$  are defined as follows

$$\theta_M = q(\tau_\phi q - 0.5) \Gamma \Delta t, \quad \text{with } q = \frac{1}{\tau_\phi + 0.5}, \quad (44)$$

$$\kappa = \frac{3\gamma \xi}{8(\phi^*)^2}, \quad A = \frac{3\gamma}{4\xi(\phi^*)^4}.$$

$L(\phi)$  is given by  $L(\phi) = \kappa \phi^* \partial_{\mathbf{n}} \phi - \frac{\pi\gamma}{4} \cos(\theta^{\text{surf}}) \cos(\frac{\pi\phi}{2\phi^*})$ .

We scale the length by  $L$ ,  $\phi$  by  $\phi^*$ , velocity by the wall speed  $V$ , time by  $L/V$ , density by  $n$ , viscosity by  $\eta$  and pressure by  $\eta V/L$ . Let us denote the scaled variable as  $\tilde{\cdot}$ , for example denote  $\tilde{t}$  as the normalized time. With the normalized interface profile thickness  $\epsilon = \frac{\xi}{2\sqrt{2}L}$ , the chemical potential is

$$\mu = -\kappa \nabla^2 \phi + 4A[\phi^3 - (\phi^*)^2 \phi] = \frac{\kappa \phi^*}{\epsilon L^2} [-\epsilon \tilde{\nabla}^2 \tilde{\phi} + \tilde{\phi}^3 / \epsilon - \tilde{\phi} / \epsilon], \quad (45)$$

where  $\tilde{\nabla} = \frac{1}{L} \nabla$ . By define the normalized chemical potential as  $\tilde{\mu} = -\epsilon \tilde{\nabla}^2 \tilde{\phi} + \tilde{\phi}^3 / \epsilon - \tilde{\phi} / \epsilon$ , we get the relationship  $\mu = \frac{\kappa \phi^*}{\epsilon L^2} \tilde{\mu}$ . With the normalized chemical potential, we can complete the normalization of Cahn–Hilliard equation as

$$\frac{\partial \tilde{\phi}}{\partial \tilde{t}} + \tilde{\nabla} \cdot (\tilde{\phi} \tilde{\mathbf{u}}) = \mathcal{L}_d \tilde{\nabla}^2 \tilde{\mu}, \quad (46)$$

where  $\mathcal{L}_d = \frac{3\theta_M \gamma}{2\sqrt{2}[\phi^*]^2 L^2 V}$ .

With  $\mathcal{R} = \frac{nVL}{\eta}$  and  $\mathcal{B} = \frac{3\gamma}{2\sqrt{2}V\eta}$ , the Navier–Stokes equations is rewritten as

$$\begin{cases} \tilde{\nabla} \cdot (\tilde{\mathbf{u}}) = 0, \\ \mathcal{R} \left\{ \frac{\partial (\tilde{\mathbf{u}})}{\partial \tilde{t}} + \tilde{\nabla} \cdot (\tilde{\mathbf{u}} \cdot \tilde{\mathbf{u}}) \right\} = -\tilde{\nabla} \tilde{p} + \tilde{\nabla}^2 \tilde{\mathbf{u}} + \tilde{\mathbf{G}}_{\text{ext}} + \mathcal{B} \tilde{\mu} \tilde{\nabla} \tilde{\phi}, \end{cases} \quad (47)$$

where  $\tilde{\mathbf{G}}_{\text{ext}} = \frac{nL^2}{V\eta} \mathbf{G}_{\text{ext}}$ . By defining  $\mathcal{V}_s = \frac{3\Lambda\gamma L}{2\sqrt{2}V\phi^*}$  and  $\mathcal{L}_s = \frac{\eta}{\beta L}$ , the boundary conditions are normalized as

$$\mathcal{L}_s^{-1} \tilde{u}_x^{\text{slip}} = -\partial_{\tilde{\mathbf{n}}} \tilde{u}_x + \mathcal{B} \tilde{L}(\tilde{\phi}) \partial_{\tilde{x}} \tilde{\phi}, \quad (48)$$

$$\frac{\partial \tilde{\phi}}{\partial \tilde{t}} + \tilde{u}_x \partial_{\tilde{x}} \tilde{\phi} = -\mathcal{V}_s \tilde{L}(\tilde{\phi}), \quad (49)$$

$$\tilde{u}_y = 0, \quad \partial_{\tilde{\mathbf{n}}} \tilde{\mu} = 0, \quad (50)$$

where  $\tilde{L}(\tilde{\phi}) = \epsilon \partial_{\tilde{\mathbf{n}}} \tilde{\phi} - \frac{\sqrt{2}\pi}{6} \cos(\theta^{\text{surf}}) \cos(\frac{\pi}{2} \tilde{\phi})$ .

## References

- [1] S. Balay, J. Brown, K. Buschelman, V. Eijkhout, W. Gropp, D. Kaushik, M. Knepley, L.C. McInnes, B. Smith, H. Zhang, PETSc Users Manual, Argonne National Laboratory, 2013.
- [2] K. Bao, Y. Shi, S. Sun, X.-P. Wang, A finite element method for the numerical solution of the coupled Cahn–Hilliard and Navier–Stokes system for moving contact line problems, *J. Comput. Phys.* 231 (2012) 8083–8099.
- [3] P.L. Bhatnagar, E.P. Gross, M. Krook, A model for collision processes in gases. I. Small amplitude processes in charged and neutral one-component systems, *Phys. Rev.* 94 (1954) 511.
- [4] V.E.B. Dussan, S.H. Davis, On the motion of a fluid–fluid interface along a solid surface, *J. Fluid Mech.* 65 (1974) 71–95.
- [5] A. Fakhari, M.H. Rahimian, Phase-field modeling by the method of lattice Boltzmann equations, *Phys. Rev. E* 81 (2010) 036707.
- [6] M. Gao, X.-P. Wang, A gradient stable scheme for a phase field model for the moving contact line problem, *J. Comput. Phys.* 231 (2012) 1372–1386.
- [7] M. Gao, X.-P. Wang, An efficient scheme for a phase field model for the moving contact line problem with variable density and viscosity, *J. Comput. Phys.* 272 (2014) 704–718.
- [8] Z. Guo, C. Zheng, B. Shi, Non-equilibrium extrapolation method for velocity and pressure boundary conditions in the lattice Boltzmann method, *Chin. Phys.* 11 (2002) 366.
- [9] Q. He, R. Glowinski, X.-P. Wang, A least-squares/finite element method for the numerical solution of the Navier–Stokes–Cahn–Hilliard system modeling the motion of the contact line, *J. Comput. Phys.* 230 (2011) 4991–5009.
- [10] X. He, S. Chen, R. Zhang, A lattice Boltzmann scheme for incompressible multiphase flow and its application in simulation of Rayleigh–Taylor instability, *J. Comput. Phys.* 152 (1999) 642–663.
- [11] T. Inamuro, T. Ogata, S. Tajima, N. Konishi, A lattice Boltzmann method for incompressible two-phase flows with large density differences, *J. Comput. Phys.* 198 (2004) 628–644.
- [12] D. Jacqmin, Calculation of two-phase Navier–Stokes flows using phase-field modeling, *J. Comput. Phys.* 155 (1999) 96–127.
- [13] D. Jamet, O. Lebaigue, N. Coutris, J. Delhay, The second gradient method for the direct numerical simulation of liquid–vapor flows with phase change, *J. Comput. Phys.* 169 (2001) 624–651.
- [14] V.M. Kendon, M.E. Cates, I. Pagonabarraga, J.C. Desplat, P. Bladon, Inertial effects in three-dimensional spinodal decomposition of a symmetric binary fluid mixture: a lattice Boltzmann study, *J. Fluid Mech.* 440 (2001) 147–203.
- [15] H.Y. Kim, J.H. Chun, The recoiling of liquid droplets upon collision with solid surfaces, *Phys. Fluids* 13 (3) (2001) 643–659.
- [16] P. Lallemand, L.S. Luo, Theory of the lattice Boltzmann method: dispersion, dissipation, isotropy, Galilean invariance, and stability, *Phys. Rev. E* 61 (2000) 6546.
- [17] T. Lee, C.L. Lin, A stable discretization of the lattice Boltzmann equation for simulation of incompressible two-phase flows at high density ratio, *J. Comput. Phys.* 206 (2005) 16–47.
- [18] Q. Li, K.H. Luo, Q.J. Kang, Y.L. He, Q. Chen, Q. Liu, Lattice Boltzmann methods for multiphase flow and phase-change heat transfer, *Prog. Energy Combust. Sci.* 52 (2016) 62–105.
- [19] Q. Li, K.H. Luo, X.J. Li, Lattice Boltzmann modeling of multiphase flows at large density ratio with an improved pseudopotential model, *Phys. Rev. E* 87 (2013) 053301.
- [20] Q. Li, K.H. Luo, X.J. Li, Forcing scheme in pseudopotential lattice Boltzmann model for multiphase flows, *Phys. Rev. E* 86 (2012) 016709.
- [21] X. Luo, X.-P. Wang, T. Qian, P. Sheng, Moving contact line over undulating surfaces, *Solid State Commun.* 139 (2006) 623–629.
- [22] D. Lyett-Brown, K.H. Luo, Improved forcing scheme in pseudopotential lattice Boltzmann methods for multiphase flow at arbitrarily high density ratios, *Phys. Rev. E* 91 (2015) 023305.
- [23] D. Lyett-Brown, K.H. Luo, Cascaded lattice Boltzmann method with improved forcing scheme for large-density-ratio multiphase flow at high Reynolds and Weber numbers, *Phys. Rev. E* 94 (2016) 053313.
- [24] S. Mukherjee, J. Abraham, Investigations of drop impact on dry walls with a lattice-Boltzmann model, *J. Colloid Interface Sci.* 312 (2) (2007) 341–354.
- [25] T. Qian, X.-P. Wang, P. Sheng, Molecular scale contact line hydrodynamics of immiscible flows, *Phys. Rev. E* 68 (2003) 016306/1.
- [26] T. Qian, X.-P. Wang, P. Sheng, Molecular hydrodynamics of the moving contact line in two-phase immiscible flows, *Commun. Comput. Phys.* 1 (2006) 1–52.
- [27] D.H. Rothman, J.M. Keller, Immiscible cellular-automaton fluids, *J. Stat. Phys.* 52 (1988) 1119–1127.
- [28] X. Shan, H. Chen, Lattice Boltzmann model for simulating flows with multiple phases and components, *Phys. Rev. E* 47 (1993) 1815.
- [29] J. Shao, C. Shu, A hybrid phase field multiple relaxation time lattice Boltzmann method for the incompressible multiphase flow with large density contrast, *Int. J. Numer. Methods Fluids* 77 (2015) 526–543.
- [30] J. Shao, C. Shu, H. Huang, Y. Chew, Free-energy-based lattice Boltzmann model for the simulation of multiphase flows with density contrast, *Phys. Rev. E* 89 (2014) 033309.
- [31] M.R. Swift, W. Osborn, J. Yeomans, Lattice Boltzmann simulation of nonideal fluids, *Phys. Rev. Lett.* 75 (1995) 830.
- [32] N. Takada, M. Misawa, A. Tomiyama, S. Hosokawa, Simulation of bubble motion under gravity by lattice Boltzmann method, *J. Nucl. Sci. Technol.* 38 (2001) 330–341.
- [33] X.-P. Wang, T. Qian, P. Sheng, Moving contact line on chemically patterned surfaces, *J. Fluid Mech.* 605 (2008) 59–78.
- [34] Y. Wang, C. Shu, H.B. Huang, C.J. Teo, Multiphase lattice Boltzmann flux solver for incompressible multiphase flows with large density ratio, *J. Comput. Phys.* 280 (2015) 404–423.
- [35] Y. Wang, C. Shu, L.M. Yang, An improved multiphase lattice Boltzmann flux solver for three-dimensional flows with large density ratio and high Reynolds number, *J. Comput. Phys.* 302 (2015) 41–58.
- [36] A. Yarin, Drop impact dynamics: splashing, spreading, receding, bouncing, *Annu. Rev. Fluid Mech.* 38 (2006) 159–192.
- [37] H. Zheng, C. Shu, Y.T. Chew, A lattice Boltzmann model for multiphase flows with large density ratio, *J. Comput. Phys.* 218 (2006) 353–371.